CHALMERS
UNIVERSITY OF TECHNOLOGY

Hybrid Codebook Design for Localization Using Electromagnetically Reconfigurable Fluid Antenna System

Citation for the original published paper (version of record):
Fadakar, A., Zhang, Y., Chen, H. et al (2026). Hybrid Codebook Design for Localization Using Electromagnetically Reconfigurable Fluid Antenna
System. IEEE Journal on Selected Topics in Signal Processing: 1-16.
http://dx.doi.org/10.1109/JSTSP.2026.3673038

(article starts on next page)

Hybrid Codebook Design for Localization Using Electromagnetically Reconfigurable Fluid Antenna System

Alireza Fadakar, *Graduate Student Member*, Yuchen Zhang, *Member, IEEE*, Hui Chen, *Member, IEEE*, Musa Furkan Keskin, *Member, IEEE*, Henk Wymeersch, *Fellow, IEEE*, and Andreas F. Molisch, *Fellow, IEEE*

***Abstract*—Electromagnetically reconfigurable fluid antenna systems (ER-FAS) introduce additional degrees of freedom in the electromagnetic (EM) domain by dynamically steering per-antenna radiation patterns, thereby enhancing power efficiency in wireless links. Unlike prior works on spatially reconfigurable FAS, which adjust element positions, ER-FAS provides direct control over each element's EM characteristics to realize on-demand beam-pattern shaping. While existing studies have exploited ER-FAS to boost spectral efficiency, this paper explores its application for downlink localization. We consider a multiple-input single-output (MISO) system in which a multi-antenna ER-FAS at the base station serves a single-antenna user equipment (UE). We consider two reconfigurability paradigms: (i) a synthesis model where each antenna generates desired beampatterns from a finite set of EM basis functions, and (ii) a finite-state selection model in which each antenna selects a pattern from a predefined set of patterns. For both paradigms, we formulate the joint baseband (BB) and EM precoder design to minimize the UE position error bound. In the synthesis case we derive low-dimensional closed-form expressions for both the BB and EM precoders. For the finite-state model we obtain closed-form BB structures and propose a low-complexity block-coordinate-descent algorithm for EM pattern selection. Analytical bounds and extensive simulations show that the proposed hybrid designs for ER-FAS substantially improve UE positioning accuracy over traditional non-reconfigurable arrays.**

***Index Terms*—Fluid antenna system, reconfigurable antennas, beamforming, beampattern, radiation pattern, localization.**

I. Introduction

A. Background

The evolution toward fifth-generation (5G) and sixth-generation (6G) networks demands orders-of-magnitude increases in data rate and capacity, driving the need for fundamental advances at the physical layer to overcome intrinsic performance limits [1], [2]. Central to this evolution is the enhancement of base station (BS) capabilities, since total system throughput mainly depends on the efficient exploitation of limited physical resources [3], [4]. While time-frequency resource allocation has been extensively optimized, spatial-domain methods, most notably multiple-input multiple-output (MIMO), offer additional degrees of freedom. However, scaling antenna aperture on mast-mounted installations encounters practical constraints (e.g., structural limits) and becomes impractical in low-density deployment scenarios. Fluid antenna systems (FAS) have recently emerged as a pivotal concept to inject new flexibility into the physical layer, positioning them as a promising enabler for 6G and beyond [2], [5]. Unlike conventional arrays with fixed element positions, fluid antenna system (FAS) can dynamically relocate the antenna element along a fluidic substrate to sample the most favorable spatial channels thereby achieving large spatial-diversity gains. Moreover, FAS can synergize with other frontier technologies such as reconfigurable intelligent surfaces (RISs) [6], massive MIMO [7], and integrated sensing and communication (ISAC) [8] to further boost network performance.

FAS can be categorized into two main categories: spatially reconfigurable FAS (SR-FAS), and electromagnetically reconfigurable FAS (ER-FAS) which are explained next.

1) SR-FAS: SR-FAS employs port-selection to reposition the radiating element, thereby exploiting spatial diversity while preserving the antenna's intrinsic electromagnetics (EM) properties [9]. SR-FAS is closely related to movable antenna (MA) technology [10]–[12]. MA and SR-FAS both share the concept of spatial reconfiguration to improve channel conditions and communication performance [9]. Specifically, MA can be regarded as a position-only variant of SR-FAS. Hence, in most cases they can be interchangeable due to their similar concepts [13]. However, SR-FAS further supports pixel-based and shape/size reconfiguration, which is common in extremely large-scale MIMO (XL-MISO) deployments [9]. This introduces mutual coupling challenges in which antenna and circuit theory plays an important part to evaluate the performance of SR-FAS, whereas mechanical or liquid-based movable designs in MA confine coupling to active radiating elements. Moreover, SR-FAS further explore shape or size adaptation for applications such as cognitive radio networks, internet of things (IoT), and body area networks [14], [15].

2) ER-FAS: ER-FAS, also referred to as reconfigurable antenna (RA), retain a fixed physical location and reshape their metallic patterns or dielectric substrates to provide on-demand control over operating frequency, polarization, and radiation

A. Fadakar and A. F. Molisch are with the Ming Hsieh Department of Electrical and Computer Engineering, University of Southern California, Los Angeles, California, USA; E-mail: {fadakarg, molisch}@usc.edu.

Y. Zhang is with the Electrical and Computer Engineering Program, Computer, Electrical and Mathematical Sciences and Engineering (CEMSE), King Abdullah University of Science and Technology (KAUST), Thuwal 23955-6900, Kingdom of Saudi Arabia; E-mail: yuchen.zhang@kaust.edu.sa.

H. Chen, M. F. Keskin, and H. Wymeersch are with the Department of Electrical Engineering, Chalmers University of Technology, Sweden; E-mails: {hui.chen, furkan, henkw}@chalmers.se.

This work is supported, in part, by the National Science Foundation (Grants 2229535 and 2106602), in part by the KAUST Global Fellowship Program under Award No. RFS-2025-6844, and in part by the Swedish Research Council (Grants 2022-03007 and 2024-04390).

pattern [1], [16], [17]. In this paper, we focus on radiation pattern-based ER-FAS. Compared to SR-FAS, the radiation properties of the ER-FAS can be dynamically adjusted in real time by altering the fluid state of the radio frequency (RF) radiator. There are various fabrication technologies to implement ER-FAS, notably pixel-based parasitic layouts [18], [19], electronically steerable parasitic array radiator (ESPAR) configurations, consisting of a single active radiator encircled by passive parasitic elements [19], [20], and liquid-metal fluidic implementations [1]. For instance in [18], a pixel-based ER-FAS with high switching speed is presented, where reconfigurability is realized by changing the interconnection states between pixels [21]. The work in [1] proposes a novel ER-FAS architecture for wireless communications, in which the radiation pattern of each array element is reconfigurable via software-controlled fluidic actuation effectively circumventing the mutual coupling effect in pixel-based fabrications.

However, these implementations present practical trade-offs. Pixel-based designs benefit from fast, electronically controlled reconfiguration and well-established fabrication processes, but can exhibit unwanted mutual coupling between active and inactive pixels [1]. By contrast, liquid-metal fluidic implementations can offer continuous geometry control and conformability that help reduce certain coupling effects and enable stretchable or conformal form factors, yet they introduce engineering challenges such as limited reconfiguration speed. It is noteworthy that the mathematical models and optimization framework developed in this paper are agnostic to the specific fabrication technology and apply to all existing classes of implementations. For consistency with prior work, we use the ER-FAS terminology throughout this paper [1].

B. Related Works

1) Wireless Localization/Sensing via SR-FAS: Radio localization has been extensively studied using fixed position antennas. More recently, preliminary studies have investigated angle-of-arrival (AOA) estimation using SR-FAS systems, which introduce additional spatial degrees of freedom [22], [23]. The advantages of SR-FAS have been also demonstrated for ISAC systems [24]–[28]. The work in [24] demonstrates that dynamically repositioning antenna elements can substantially enhance spectral efficiency, beamforming precision, coverage adaptability, and transmit-power efficiency in ISAC systems. The work in [27] jointly optimizes antenna positions in SR-FAS and dual-functional beamforming via alternating optimization to maximize sensing signal-to-noise ratio (SNR) under movement and interference constraints, with robust extensions to imperfect channel state information (CSI).

2) Wireless Localization/Sensing via ER-FAS: Existing ER-FAS works for sensing often adopt ESPAR architectures. By dynamically adjusting the reactive loads of the parasitic elements, each element of the ER-FAS can directionally steer its beampatterns, supporting AOA estimation [29]–[37]. The work in [29] is one of the earliest applications of ER-FAS for AOA estimation using the multiple signal classification (MUSIC) algorithm. In [30], [31], the authors develop compressive-sensing frameworks for ER-FAS-enabled AOA estimation via sparse representations, and [36] proposes a novel single-anchor indoor localization scheme based on ER-FAS. In [32], 2D-AOA estimation is achieved using only received signal strength (RSS) measurements, while [33] demonstrates that interpolating calibrated radiation patterns can enhance ER-FAS-based AOA estimation in wireless sensor network (WSN) nodes. The authors in [34] further improve performance by applying support-vector classification to RSS outputs. More recently, [35] illustrates rapid optimal beam selection at mmWave frequencies, and [37] presents a calibration-free single-anchor indoor localization algorithm for BSs equipped with ER-FAS.

C. Motivation

Although ER-FAS enabled systems have demonstrated promising gains in communication-centric applications [1], [3], [7], [19], they still remain in the early stages of development, and their impact on wireless sensing particularly localization has yet to be examined. In particular, the existing works on ER-FAS in wireless sensing and localization are mostly limited to single-antenna BS. Thus, they cannot readily extend to modern multi-antenna systems in 5G, 6G, and beyond, where integrating FAS requires the joint optimization of EM and baseband (BB) precoders [2]. Moreover, the existing works yield suboptimal performance due to heuristic EM precoding design without discussion on optimal designs and theoretical bounds. To the best of our knowledge, this is the first study to jointly optimize both BB and EM precoders in a multiple input single output (MISO) system employing ER-FAS to maximize downlink localization accuracy in a wideband orthogonal frequency division multiplexing (OFDM) wireless system.

D. Contributions

The key contributions are summarized as follows:

- We rigorously derive the signal models and corresponding Fisher information matrix (FIM) for localization with ER-FAS under two reconfigurability paradigms: (i) the synthesis model, in which each antenna synthesizes a desired beampattern from a finite set of basis functions; and (ii) the finite-state selection model, in which each antenna selects one pattern from a discrete library of physically realizable patterns. For both cases, we present theoretical bounds on the achievable localization accuracy.
- For the synthesis model, assuming perfect knowledge of the user equipment (UE) position, we derive the optimal low-dimensional structures of the BB and EM precoders, which reveal that only three distinct beams are required. Leveraging these solutions, we then develop a robust, codebook-based design that maintains high localization accuracy under UE-position uncertainty.
- For the finite-state selection model with perfect UE-position knowledge, we decouple the BB and EM precoder designs. In particular, first, by assuming fixed EM precoders, we derive the optimal low-dimensional structure of the BB precoders and show that only three beams are needed similar to the synthesis case. Building on our results from the synthesis case, we then introduce a low-complexity block-coordinate descent (BCD)

algorithm to optimize the EM precoders for each of these three beams. Finally, by integrating these closed-form and iterative strategies, we develop a robust, codebook-based scheme that maintains high localization accuracy under UE-position uncertainty.

- We develop a low-complexity maximum likelihood (ML) based localization algorithm and perform comprehensive simulations to evaluate the position error bound (PEB) and localization root mean square error (RMSE), benchmarking against traditional non-reconfigurable arrays. Our results demonstrate substantial gains compared to existing works utilizing traditional non-reconfigurable arrays under both the synthesis and finite-state selection paradigms. For the finite-state selection case, we adopt the physically realizable pattern library obtained in [1].

Notation: Matrices are denoted by boldface uppercase letters (e.g., $\mathbf{X}$) and vectors by boldface lowercase letters (e.g., $\mathbf{x}$). The superscripts $(\cdot)^{\mathsf{T}}$, $(\cdot)^{\mathsf{H}}$, and $(\cdot)^{-1}$ denote transpose, Hermitian (conjugate transpose), and matrix inverse, respectively. The expression $[\mathbf{x}_1, \ldots, \mathbf{x}_n]$ denotes horizontal concatenation of vectors $\mathbf{x}_1, \ldots, \mathbf{x}_n$, $\mathrm{diag}(\mathbf{x})$ is the diagonal matrix with the entries of $\mathbf{x}$ on its main diagonal, and $\mathrm{blkdiag}\{\mathbf{A}_1, \ldots, \mathbf{A}_n\}$ is a block diagonal matrix with diagonal blocks $\{\mathbf{A}_i\}_{i=1}^n$. The $n \times n$ identity matrix is $\mathbf{I}_n$. The notations $\|\mathbf{x}\|$ and $\|\mathbf{x}\|_0$ denote the ℓ_2 (Euclidean) norm and the ℓ_0 norm (the number of nonzero entries of $\mathbf{x}$), respectively. We use $\mathbf{A} \otimes \mathbf{B}$, and $\mathbf{A} \odot \mathbf{B}$, for the Kronecker product, and Hadamard product, respectively. Finally, $\mathbf{\Pi}_{\mathbf{X}} = \mathbf{X}(\mathbf{X}^{\mathsf{H}}\mathbf{X})^{-1}\mathbf{X}^{\mathsf{H}}$ denotes the orthogonal projector onto the column space of $\mathbf{X}$, and $\mathbf{\Pi}_{\mathbf{X}}^{\perp} = \mathbf{I} - \mathbf{\Pi}_{\mathbf{X}}$.

II. System and Signal Model

As shown in Fig. 1a, we consider a MISO wireless system, comprising an ER-FAS at the BS with a uniform planar array (UPA) structure consisting of $M = M^h M^v$ antennas with M^h and M^v being the number of rows and columns, respectively. Each element of the ER-FAS can choose one of several predefined states or radiation patterns in the finite-state selection model or synthesize the desired pattern. For instance, in Fig. 1b, the heatmaps of 8 states are shown illustrating the radiation patterns in the finite-state selection model. The details will be provided in Sec. III. Furthermore, we assume a UE equipped with a single antenna, and I multipath components (MPCs) to model interference based on a geometric channel model which will be detailed in the next subsection. It is assumed that the BS transmits N_t OFDM downlink transmissions to the UE, each with N_s subcarriers.

The received signal in the t-th symbol on the n-th subcarrier is given by:

$$y_{t,n} = \sqrt{P}\mathbf{h}_{t,n}^{\mathsf{T}}\mathbf{f}_t + v_{t,n}, \tag{1}$$

where P denotes the transmit power, and the vector $\mathbf{f}_t \in \mathbb{C}^M$ denotes the BS BB precoder for the t-th transmission. To keep the transmit power P constant over the entire transmissions the BB precoders are assumed to satisfy $\sum_{t=1}^{N_t} \mathbf{f}_t^{\mathsf{H}}\mathbf{f}_t = 1$. Moreover, $\mathbf{h}_{t,n} \in \mathbb{C}^M$ represents the wireless channel between the BS and UE, while $v_{t,n} \sim \mathcal{CN}(0, \sigma_v^2)$ denotes the additive white Gaussian noise. It is noteworthy that the dependency of the channel on the time index t is due to the time-variant nature of ER-FAS which will be explained later.

Based on the geometric channel model, assuming the presence of a line-of-sight (LoS) path and I non-line-of-sight (NLoS) paths, the channel vector $\mathbf{h}_{t,n}$ can be expressed as [1], [3], [38]:

$$\mathbf{h}_{t,n} = \sum_{i=0}^{I} \alpha_i e^{-j2\pi\tau_i n\Delta f}\mathbf{q}_t(\boldsymbol{\theta}_i), \tag{2}$$

where $i = 0$ corresponds to LoS component, $\alpha_i = \rho_i e^{j\varphi_i}$ represents the complex gain of the i-th path, with ρ_i and φ_i denoting its modulus and phase components, respectively. Moreover, $\mathbf{q}_t(\boldsymbol{\theta}) \in \mathbb{C}^M$ represents the joint contribution of the array response vector (ARV) and the radiation patterns of the antennas at the BS in the t-th transmission for a given angle-of-departure (AOD) $\boldsymbol{\theta}$, and is defined as follows:

$$\mathbf{q}_t(\boldsymbol{\theta}) = \mathbf{g}_t(\boldsymbol{\theta}) \odot \mathbf{a}(\boldsymbol{\theta}), \tag{3}$$

where $\mathbf{g}_t(\boldsymbol{\theta}) \in \mathbb{C}^M$ represents the complex radiation patterns of the ER-FAS elements, and $\mathbf{a}(\boldsymbol{\theta})$ denotes the ARV of the corresponding array.

In (2), τ_i denotes the delay of the i-th path with $i = 0$ accounting for the LoS path:

$$\tau_0 = \frac{\|\mathbf{p}_u - \mathbf{p}_b\|}{c}, \ \tau_i = \frac{\|\mathbf{p}_u - \mathbf{p}_s^{(i)}\| + \|\mathbf{p}_s^{(i)} - \mathbf{p}_b\|}{c}, \tag{4}$$

where $\mathbf{p}_u \in \mathbb{R}^3$ and $\mathbf{p}_b \in \mathbb{R}^3$ denote the position of the UE and the center of the BS, respectively. Moreover, $\mathbf{p}_s^{(i)} \in \mathbb{R}^3$ denotes the position of the i-th multipath component (MPC) characterizing the corresponding NLoS path.

The vector $\boldsymbol{\theta}_i = [\theta_i^{\text{el}}, \theta_i^{\text{az}}]^{\mathsf{T}}$ represents the elevation and azimuth AOD in the i-th path where $i = 0$ corresponds to the LoS path. These angles can be obtained as follows:

$$\theta_0^{\text{el}} = \arccos\left(\frac{[\mathbf{p}_{u;b}]_3}{\|\mathbf{p}_{u;b}\|}\right), \ \theta_0^{\text{az}} = \text{arctan2}([\mathbf{p}_{u;b}]_2, [\mathbf{p}_{u;b}]_1), \tag{5}$$

$$\theta_i^{\text{el}} = \arccos\left(\frac{[\mathbf{p}_{s;b}^{(i)}]_3}{\|\mathbf{p}_{s;b}^{(i)}\|}\right), \ \theta_i^{\text{az}} = \text{arctan2}([\mathbf{p}_{s;b}^{(i)}]_2, [\mathbf{p}_{s;b}^{(i)}]_1), \tag{6}$$

where $\mathbf{p}_{u;b} = \mathbf{R}_b^{\top}(\mathbf{p}_u - \mathbf{p}_b)$, and $\mathbf{p}_{s;b}^{(i)} = \mathbf{R}_b^{\top}(\mathbf{p}_s^{(i)} - \mathbf{p}_b)$ with $\mathbf{R}_b \in \mathbb{R}^{3\times 3}$ being the rotation matrix corresponding to the orientation of the BS. The ARV $\mathbf{a}(\boldsymbol{\theta})$ is defined as:

$$\mathbf{a}(\boldsymbol{\theta}) = e^{-j2\pi\omega^h \mathbf{k}(M^h)} \otimes e^{-j2\pi\omega^v \mathbf{k}(M^v)}, \tag{7}$$

where $\mathbf{k}(M) = [0, \ldots, M-1]^{\mathsf{T}}$, and ω^h and ω^v represent the spatial horizontal and vertical frequencies, respectively. As shown in Fig. 1a, if the UPA is positioned on the YoZ plane of the local Cartesian coordinate system of the BS, then

$$\omega^h = d\sin(\theta^{\text{az}})\sin(\theta^{\text{el}})/\lambda, \ \omega^v = d\cos(\theta^{\text{el}})/\lambda, \tag{8}$$

where d, denotes the distance between two adjacent elements, and λ is the wavelength. Moreover, $\theta^{\text{az}}, \theta^{\text{el}}$ represent the azimuth and elevation angles in the BS's local Cartesian coordinates. Azimuth $\theta^{\text{az}} \in [-\pi, \pi)$ is measured from $+y$ toward $+x$, and elevation $\theta^{\text{el}} \in [0, \pi]$ is the angle with respect to $+z$ direction.

III. Modeling Reconfigurable Gains

The reconfigurability of the complex amplitude of ER-FAS radiation patterns $\mathbf{g}_t(\boldsymbol{\theta})$ in (3) can be captured via two complementary modeling paradigms [7]. In the first, an idealized ER-FAS is assumed to synthesize arbitrary beampatterns on

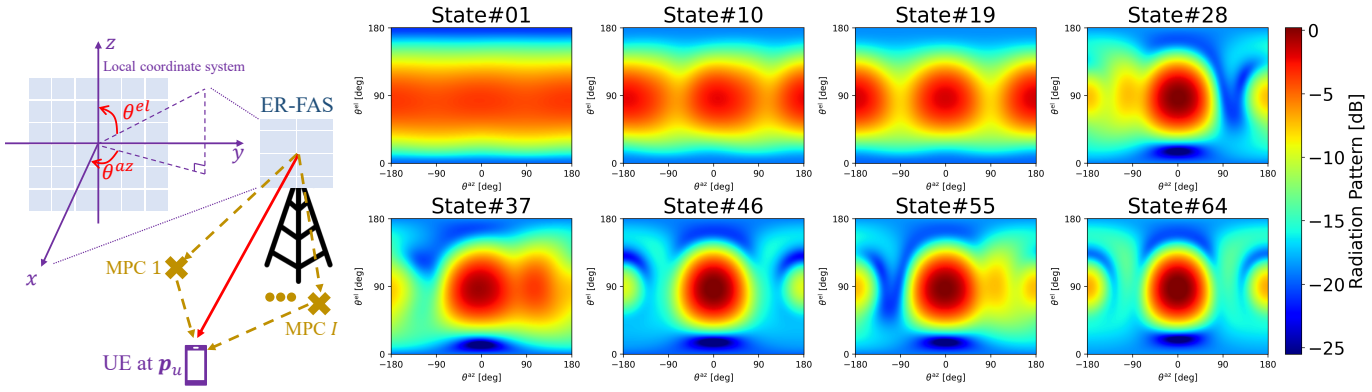

Fig. 1: (a) Considered ER-FAS assisted system. This paper aims to jointly optimizing BB and EM precoders to maximize UE localization performance. (b) The 2D heatmap radiation patterns (i.e., $\bar{b}_s(\boldsymbol{\theta})$) of 8 states among the total of $S_{\max} = 64$ states. In this paper, the physically realizable patterns in [1] are used for simulations.

demand by projecting onto a pre-defined set of orthonormal basis functions [3], [19]. In the second model, motivated by practical implementations, each antenna element toggles among a finite collection of discrete states, with each state producing a unique radiation response. For instance, a concrete hardware realization is described in [1]. In what follows, we incorporate both the synthesis and the finite-state models into the unified signal framework of (3).

A. Synthesis Model

This model assumes that each element of the ER-FAS is capable of synthesizing radiation patterns. A given beampattern can be described either in the angular domain [19] or via a spherical-harmonic expansion [3]. While the angular-domain formulation often leads to prohibitively large channel matrices, the spherical-domain representation exploits the band-limited nature of practical patterns to achieve a more compact parametrization [7]. Consequently, this work also adopts the spherical-domain framework which is detailed next.

Let $\mathbf{b}(\boldsymbol{\theta}) = [b_1(\boldsymbol{\theta}), \ldots, b_Q(\boldsymbol{\theta})]^{\mathsf{T}}$ denote a vector of Q orthonormal basis functions. Hence, the radiation response of the m-th antenna element of the ER-FAS at the t-th transmission is written as

$$\big[\mathbf{g}_t(\boldsymbol{\theta})\big]_m = \mathbf{e}_{m,t}^{\mathsf{H}} \mathbf{b}(\boldsymbol{\theta}), \tag{9}$$

where $\mathbf{e}_{m,t} \in \mathbb{C}^Q$ is the EM precoder vector that assigns weights to the basis functions to generate the desired beampattern of the m-th element of the ER-FAS during the t-th transmission. To ensure compliance with the energy conservation law, we assume that $\|\mathbf{e}_{m,t}\|^2 = 1$ [3] (see Appendix A-C for proof). Let the coefficient matrix $\mathbf{E}_t \in \mathbb{C}^{M \times MQ}$ be defined as

$$\mathbf{E}_t = \text{blkdiag}\big\{\mathbf{e}_{1,t}^{\mathsf{H}}, \ldots, \mathbf{e}_{M,t}^{\mathsf{H}}\big\}. \tag{10}$$

Then, (3) can be rewritten as:

$$\mathbf{q}_t(\boldsymbol{\theta}) = \mathbf{E}_t\big(\mathbf{a}(\boldsymbol{\theta}) \otimes \mathbf{b}(\boldsymbol{\theta})\big) = \mathbf{E}_t\, \mathbf{c}(\boldsymbol{\theta}), \tag{11}$$

where $\mathbf{c}(\boldsymbol{\theta}) = \mathbf{a}(\boldsymbol{\theta}) \otimes \mathbf{b}(\boldsymbol{\theta}) \in \mathbb{C}^{MQ}$. Substituting (11) into (2), then that results into (1), and finally stacking all N_s symbols within the t-th time transmission yields

$$\mathbf{y}_t = \sum_{i=0}^{I} \sqrt{P}\, \alpha_i\, \mathbf{d}(\tau_i)\, \mathbf{c}(\boldsymbol{\theta}_i)^{\mathsf{T}}\, \mathbf{E}_t^{\mathsf{T}}\, \mathbf{f}_t + \mathbf{v}_t\,, \tag{12}$$

where $\mathbf{d}(\tau) \in \mathbb{C}^{N_s}$ denotes the delay steering vector defined as:

$$\mathbf{d}(\tau) = [1, e^{-j2\pi\Delta f \tau}, \ldots, e^{-j2\pi(N_s-1)\Delta f \tau}]^{\mathsf{T}}. \tag{13}$$

In this paper, we adopt spherical harmonious orthogonal decomposition (SHOD) functions [39] for basis functions due to their simplicity. Under the SHOD paradigm, any radiation pattern admits an infinite-series expansion in spherical harmonics [3]. In this paper, we truncate these bases to the first Q basis functions for simulations. Further details on the definition of $b_n(\boldsymbol{\theta})$ via SHOD are provided in Appendix A.

Remark 1. ***Basis-agnostic methodology:*** *While SHOD bases are used for simulations, our optimization and estimation techniques impose no special structure on these bases. Consequently, any complete set of orthonormal functions could be substituted in future work. Although SHOD may not yet be fully realized in practical hardware, it establishes the ultimate performance bound for ER-FAS implementations [3], [7]. Early efforts, e.g., [20], [40], have explored the design of physically realizable basis functions (which are also referred to as characteristic modes). However, this area is in its early stages and is an important direction for future research.*

B. Finite State Selection Model

The finite-state selection model provides the most faithful representation of practical hardware implementations [7]. We assume a set of S candidate beampatterns, each parameterized by $\boldsymbol{\theta}$ and arranged as $\bar{\mathbf{b}}(\boldsymbol{\theta}) = \big[\bar{b}_1(\boldsymbol{\theta}), \ldots, \bar{b}_S(\boldsymbol{\theta})\big]^{\mathsf{T}} \in \mathbb{R}_+^S$. Accordingly, the radiation response of the m-th element of the ER-FAS in the t-th transmission is expressed as

$$\big[\mathbf{g}_t(\boldsymbol{\theta})\big]_m = \bar{\mathbf{e}}_{m,t}^{\mathsf{T}}\, \bar{\mathbf{b}}(\boldsymbol{\theta}), \tag{14}$$

where $\bar{\mathbf{e}}_{m,t} \in \{0,1\}^S$ is a one-hot selection vector satisfying $\|\bar{\mathbf{e}}_{m,t}\|_0 = 1$, i.e., exactly one entry equals 1. Moreover, we assume that the total power of each state equals 1 i.e., $\int_0^{2\pi}\int_0^{\pi} |\bar{b}_s(\boldsymbol{\theta})|^2 \sin\theta^{\text{el}}\, d\theta^{\text{el}}\, d\theta^{\text{az}} = 1$. This constraint ensures the energy conservation law (see Appendix A-C for proof).

Analogous to the synthesis case, we introduce the discrete-state coefficient matrix for the t-th transmission as:

$$\bar{\mathbf{E}}_t = \text{blkdiag}\big\{\bar{\mathbf{e}}_{1,t}^{\mathsf{T}}, \ldots, \bar{\mathbf{e}}_{M,t}^{\mathsf{T}}\big\} \in \{0,1\}^{M \times MS}. \tag{15}$$

Hence, (3) can be represented as

$$\mathbf{q}_t(\boldsymbol{\theta}) = \overline{\mathbf{E}}_t \left(\mathbf{a}(\boldsymbol{\theta}) \otimes \overline{\mathbf{b}}(\boldsymbol{\theta})\right) = \overline{\mathbf{E}}_t\, \overline{\mathbf{c}}(\boldsymbol{\theta}), \tag{16}$$

where $\overline{\mathbf{c}}(\boldsymbol{\theta}) = \mathbf{a}(\boldsymbol{\theta}) \otimes \overline{\mathbf{b}}(\boldsymbol{\theta}) \in \mathbb{C}^{MS}$. By inserting (16) into (2), then substituting the result into (1) and collecting the N_s symbols over the t-th time frame, we obtain

$$\mathbf{y}_t = \sum_{i=0}^{I} \sqrt{P}\, \alpha_i\, \mathbf{d}(\tau_i)\, \overline{\mathbf{c}}(\boldsymbol{\theta}_i)^{\mathsf{T}}\, \overline{\mathbf{E}}_t^{\mathsf{T}}\, \mathbf{f}_t \;+\; \mathbf{v}_t. \tag{17}$$

Remark 2. ***Pattern generation vs. state selection:*** *Both the synthesis and finite-state selection models lead to analogous compact signal representations in* (12) *and* (17)*, respectively, differing only in their physical interpretation and underlying constraints. The synthesis model uses continuous coefficients* $\{\mathbf{E}_t\}_{t=1}^{N_t}$ *to generate beampatterns, whereas the finite-state selection model uses binary selection matrices* $\{\overline{\mathbf{E}}_t\}_{t=1}^{N_t}$ *to switch among a finite library of predefined patterns.*

C. Fisher Information Analysis

In this section, we derive the FIM for the 3D UE position and obtain the corresponding Cramér-Rao bound (CRB). These bounds serve as the objective for the joint design of the BB and EM precoders. Owing to the parallel structure of the synthesis and finite-state selection models introduced in Sec. III, we present the derivation for the synthesis case only. The results for the finite-state selection model can be readily obtained by replacing $\mathbf{c}(\boldsymbol{\theta}_i)$ with $\overline{\mathbf{c}}(\boldsymbol{\theta}_i)$ and $\mathbf{E}_t$ with $\overline{\mathbf{E}}_t$.

1) FIM in Channel Domain: Similar to [38], [41], and due to the considerable path loss associated with NLoS components as well as the unknown number of such paths, we treat the NLoS paths as interference. Thus, only considering the LoS components with index 0 in (12), we define the channel parameter vector $\boldsymbol{\gamma} \in \mathbb{R}^5$ as:

$$\boldsymbol{\gamma} = [\theta^{\text{el}}, \theta^{\text{az}}, \tau, \rho, \varphi]^{\mathsf{T}}, \tag{18}$$

where the index 0 are dropped for notational simplicity. Then, the (i,j)-th element of the FIM $\mathbf{J}_{\boldsymbol{\gamma}} \in \mathbb{C}^{5\times 5}$ can be obtained as [8], [41], [42]:

$$[\mathbf{J}_{\boldsymbol{\gamma}}]_{i,j} = \frac{2}{\sigma_v^2} \sum_{t=1}^{N_t} \Re\left\{ \left(\frac{\partial \mathbf{x}_t}{\partial \gamma_i}\right)^{\mathsf{H}} \left(\frac{\partial \mathbf{x}_t}{\partial \gamma_j}\right) \right\}, \tag{19}$$

where $\mathbf{x}_t = \sqrt{P}\alpha\, \mathbf{d}(\tau)\mathbf{c}(\boldsymbol{\theta})^{\mathsf{T}}\mathbf{E}_t^{\mathsf{T}}\mathbf{f}_t$ denotes the multipath- and noise-free version of (12) at the position $\mathbf{p}_u$.

2) FIM in Position Domain: To compute the FIM $\mathbf{J}_{\boldsymbol{\eta}} \in \mathbb{R}^{5\times 5}$ corresponding to the state-space parameter vector

$$\boldsymbol{\eta} = \left[\mathbf{p}_{\text{u}}^{\mathsf{T}},\, \rho,\, \varphi\right]^{\mathsf{T}}, \tag{20}$$

we employ a Jacobian-based transformation. Specifically, the Jacobian matrix $\mathbf{T} = \frac{\partial \boldsymbol{\gamma}^{\mathsf{T}}}{\partial \boldsymbol{\eta}} \in \mathbb{R}^{5\times 5}$ is used to map the FIM from the channel parameter domain to the state domain via the relation $\mathbf{J}_{\boldsymbol{\eta}} = \mathbf{T}\mathbf{J}_{\boldsymbol{\gamma}}\mathbf{T}^{\mathsf{T}}$. Based on this transformed FIM, the PEB at the location $\mathbf{p}_{\text{u}}$ is given by:

$$\text{PEB} = \text{tr}([\mathbf{J}_{\boldsymbol{\eta}}^{-1}]_{1:3,1:3}). \tag{21}$$

IV. Hybrid Codebook Design: Synthesis Model

In this section, first we formulate the hybrid beamforming design optimization problem using the synthesis ER-FAS model explained in Sec. III-A. Then, we design a codebook containing N_t beams.

A. Optimal Structure of Precoders

Assuming a *perfect knowledge* of $\boldsymbol{\eta}$ in (20), we formulate the optimization problem to jointly design the EM precoders $\{\mathbf{E}_t\}_{t=1}^{N_t}$ and BB precoders $\{\mathbf{f}_t\}_{t=1}^{N_t}$ to minimize the PEB. To this end, we formulate the problem as follows:

$$\min_{\{\mathbf{E}_t, \mathbf{f}_t\}_{t=1}^{N_t}} \quad \text{PEB}\left(\{\mathbf{E}_t\}_{t=1}^{N_t}, \{\mathbf{f}_t\}_{t=1}^{N_t};\; \boldsymbol{\eta}\right) \tag{22a}$$

$$\text{s.t.} \quad \left\|[\mathbf{E}_t]_{m,[(m-1)Q+1:mQ]}\right\|^2 = 1, \tag{22b}$$

$$\sum_{t=1}^{N_t} \mathbf{f}_t^{\mathsf{H}}\mathbf{f}_t = 1, \tag{22c}$$

$$m = 1, \ldots, M,\; t = 1, \ldots, N_t,$$

where the constraint (22b) is equivalent to the constraint $\|\mathbf{e}_{m,t}\|^2 = 1$ discussed in Sec. III-A. The constraint (22c) ensures that P in (12) is the total transmitted power across all transmissions. The optimization problem (22) is high dimensional due to coupled EM and BB precoders. To make (22) more tractable and simpler, we define the vectors $\{\mathbf{w}_t\}_{t=1}^{N_t}$ as follows:

$$\mathbf{w}_t = \mathbf{E}_t^{\mathsf{T}}\mathbf{f}_t \in \mathbb{C}^{MQ}. \tag{23}$$

With this definition, to tackle (22), we first find the *low-dimensional structure* of the vectors $\{\mathbf{w}_t\}_{t=1}^{N_t}$, and then, we will obtain the optimal structures for the EM and BS precoders. First, we state the following lemma:

Lemma 1. *The PEB defined in* (21) *is a convex function with respect to the matrix* $\mathbf{W} = \sum_{t=1}^{N_t} \mathbf{W}_t$ *where* $\mathbf{W}_t = \mathbf{w}_t\mathbf{w}_t^{\mathsf{H}}$.

Proof. Assuming $\mathbf{W} = \sum_{t=1}^{N_t} \mathbf{W}_t$, the entries of the first row of the FIM $\mathbf{J}_{\boldsymbol{\gamma}}$ in (19) can be obtained as:

$$A\Re\{\mathbf{c}^{(2)}(\boldsymbol{\theta})^{\mathsf{T}}\mathbf{W}\mathbf{c}^{(2)}(\boldsymbol{\theta})^*\},\; A\Re\{\mathbf{c}^{(3)}(\boldsymbol{\theta})^{\mathsf{T}}\mathbf{W}\mathbf{c}^{(2)}(\boldsymbol{\theta})^*\},$$
$$\frac{A\dot{N}_s}{N_s}\Re\{\mathbf{c}^{(1)}(\boldsymbol{\theta})^{\mathsf{T}}\mathbf{W}\mathbf{c}^{(2)}(\boldsymbol{\theta})^*\},\; \frac{A}{\rho}\Re\{\mathbf{c}^{(1)}(\boldsymbol{\theta})^{\mathsf{T}}\mathbf{W}\mathbf{c}^{(2)}(\boldsymbol{\theta})^*\},$$
$$A\Re\{j\mathbf{c}^{(1)}(\boldsymbol{\theta})^{\mathsf{T}}\mathbf{W}\mathbf{c}^{(2)}(\boldsymbol{\theta})^*\},$$

where $A = \frac{2PN_s\rho^2}{\sigma_v^2}$, $\dot{N}_s = \mathbf{d}(\tau)^{\mathsf{H}}\frac{\partial \mathbf{d}(\tau)}{\partial \tau}$, and:

$$\mathbf{c}^{(1)}(\boldsymbol{\theta}) = \mathbf{c}(\boldsymbol{\theta}),\; \mathbf{c}^{(2)}(\boldsymbol{\theta}) = \frac{\partial \mathbf{c}(\boldsymbol{\theta})}{\partial \theta^{\text{el}}},\; \mathbf{c}^{(3)}(\boldsymbol{\theta}) = \frac{\partial \mathbf{c}(\boldsymbol{\theta})}{\partial \theta^{\text{az}}}. \tag{24}$$

The elements in other rows can be obtained in a similar manner. Hence, the elements of the FIM $\mathbf{J}_{\boldsymbol{\gamma}}$ defined in (19) linearly depend on $\mathbf{W}$. Thus, according to the composition rule [43], the PEB in (21) is a convex function of this matrix.

Thus, to transform the non-convex optimization problem (22) into a convex one, first we represent it in terms of $\mathbf{W}$, and assume that there exists feasible BS and EM precoders $\{\mathbf{E}_t, \mathbf{f}_t\}_{t=1}^{N_t}$ for the optimal matrix $\mathbf{W}$. Hence, with this assumption, we drop the constraints (22b), and (22c), and reformulate (22) as follows:

$$\min_{\mathbf{W}} \quad \text{PEB}\left(\mathbf{W}; \boldsymbol{\eta}\right) \tag{25a}$$

$$\text{s.t.} \quad \text{tr}\left(\mathbf{W}\right) = 1, \tag{25b}$$

$$\text{rank}(\mathbf{W}) \le N_t\,, \tag{25c}$$

where (25b) is the equivalent power constraint to (22c) [1]. Then, we relax the problem by dropping the rank constraint in (25c)

[1]Since $\|\mathbf{e}_{m,t}\|^2 = 1$, we have $\text{tr}(\mathbf{W}_t) = \mathbf{w}_t^{\mathsf{H}}\mathbf{w}_t = \mathbf{f}_t^{\mathsf{H}}\mathbf{f}_t$. Combining this with (22c), we obtain $\text{tr}(\mathbf{W}) = \sum_{t=1}^{N_t} \text{tr}(\mathbf{W}_t) = \sum_{t=1}^{N_t} \mathbf{f}_t^{\mathsf{H}}\mathbf{f}_t = 1$.

to obtain a convex optimization problem. To achieve low-complexity optimization, we use the low-dimensional structure of the optimal matrix $\mathbf{W}$ in the following proposition.

Proposition 1. *The optimal matrix* $\mathbf{W}$ *can be represented as:*

$$\mathbf{W} = \mathbf{C}_w \mathbf{\Xi} \mathbf{C}_w^{\mathsf{H}} \tag{26}$$

where $\mathbf{\Xi} \in \mathbb{C}^{3\times 3}$ *is a positive semidefinite (PSD) matrix, and* $\mathbf{C}_w = [\mathbf{c}^{(1)}(\boldsymbol{\theta})^*, \mathbf{c}^{(2)}(\boldsymbol{\theta})^*, \mathbf{c}^{(3)}(\boldsymbol{\theta})^*] \in \mathbb{C}^{MQ\times 3}$.

Proof. See Appendix B.

Proposition 2. *Based on the optimal low-dimensional structure of the matrix* $\mathbf{W} = \sum_{t=1}^{N_t} \mathbf{W}_t$ *in Prop. 1, we propose to use the following* $N_t = 3$ *codewords* $\{\mathbf{w}_i\}_{i=1}^3$ *to achieve the approximate optimal value of* (25)*:*

$$\widehat{\mathbf{w}}_i = \sqrt{\delta_i} \frac{\mathbf{c}^{(i)}(\boldsymbol{\theta})^*}{\|\mathbf{c}^{(i)}(\boldsymbol{\theta})\|}, \tag{27}$$

where $1 \geq \delta_i \geq 0$ *is the portion of power dedicated to the* i*-th codeword which should satisfy the inequality* $\delta_1 + \delta_2 + \delta_3 \leq 1$*. For* $i \in \{1, 2, 3\}$*, the corresponding BB and EM precoders can be obtained as:*

$$[\hat{\mathbf{f}}_i]_m = \sqrt{\delta_i} \frac{\|\mathbf{c}_m^{(i)}(\boldsymbol{\theta})\|}{\|\mathbf{c}^{(i)}(\boldsymbol{\theta})\|} e^{j\psi_{m,i}}, \ \hat{\mathbf{e}}_{m,i} = \frac{\mathbf{c}_m^{(i)}(\boldsymbol{\theta})}{\|\mathbf{c}_m^{(i)}(\boldsymbol{\theta})\|} e^{-j\psi_{m,i}}, \tag{28}$$

where $\mathbf{c}_m^{(i)}(\boldsymbol{\theta}) = [\mathbf{c}^{(i)}(\boldsymbol{\theta})]_{((m-1)Q+1):mQ}$*, and* $\{\psi_{m,i}\}_{m=1,i=1}^{M,3}$ *are arbitrary phases.*

Proof. See Appendix C.

B. Proposed Codebook

In Sec. IV-A, we obtained a low-complexity joint BB and EM codebook design based on the optimal solutions of (22), that minimizes the PEB under perfect knowledge of state parameters including UE position. However, in practice the UE position may not be available due to measurement errors. Let $\boldsymbol{\mathcal{U}}$ denote a 3D region accounting for the UE position uncertainty region. To obtain a robust design under UE position uncertainty, assuming $\{\boldsymbol{\theta}_\ell\}_{\ell=1}^L$ are uniformly spaced AODs covering the uncertainty region, based on Prop. 2, we propose the following codebook consisting of $N_t = 3L$ codewords for the BB and EM precoders:

$$\boldsymbol{\mathcal{F}} = \left\{ \sqrt{\delta_{3\ell-2}}\hat{\mathbf{f}}_1(\boldsymbol{\theta}_\ell), \sqrt{\delta_{3\ell-1}}\hat{\mathbf{f}}_2(\boldsymbol{\theta}_\ell), \sqrt{\delta_{3\ell}}\hat{\mathbf{f}}_3(\boldsymbol{\theta}_\ell) \right\}_{\ell=1}^{L},$$
$$\boldsymbol{\mathcal{E}} = \left\{ \widehat{\mathbf{E}}_1(\boldsymbol{\theta}_\ell), \widehat{\mathbf{E}}_2(\boldsymbol{\theta}_\ell), \widehat{\mathbf{E}}_3(\boldsymbol{\theta}_\ell) \right\}_{\ell=1}^{L}, \tag{29}$$

where $\widehat{\mathbf{E}}_i$ is obtained using (10). The equivalent representation of this codebook based on vectors $\widehat{\mathbf{w}}_i$ in (27) can be expressed as:

$$\boldsymbol{\mathcal{W}} = \left\{ \sqrt{\delta_{3\ell-2}}\widehat{\mathbf{w}}_1(\boldsymbol{\theta}_\ell), \sqrt{\delta_{3\ell-1}}\widehat{\mathbf{w}}_2(\boldsymbol{\theta}_\ell), \sqrt{\delta_{3\ell}}\widehat{\mathbf{w}}_3(\boldsymbol{\theta}_\ell) \right\}_{\ell=1}^{L}. \tag{30}$$

In (29) and (30), we separate the power-allocation coefficients to emphasize that they are the only remaining parameters to be optimized, and to streamline the exposition of their optimization procedure in the next subsection.

C. Power Allocation Optimization

The power allocation optimization problem inside an uncertainty region $\boldsymbol{\mathcal{U}}$ can be formulated as:

$$\min_{\{\delta_t\}_{t=1}^{N_t}} \max_{\boldsymbol{p}_u \in \boldsymbol{\mathcal{U}}} \ \mathrm{PEB}\left(\{\delta_t \widehat{\mathbf{W}}_t\}_{t=1}^{N_t};\ \boldsymbol{\eta}(\mathbf{p}_u)\right) \tag{31a}$$

$$\text{s.t.} \quad \delta_t \geq 0,\ \sum_{t=1}^{N_t} \delta_t = 1, \tag{31b}$$

where $\delta_t \widehat{\mathbf{W}}_t = \delta_t \widehat{\mathbf{w}}_t \widehat{\mathbf{w}}_t^{\mathsf{H}}$ is the covariance matrix of the t-th codeword in (30). First, we obtain the semi-infinite version of this optimization problem by using its epigraph form [43]:

$$\min_{\varrho, \{\delta_t\}_{t=1}^{N_t}} \quad \varrho \tag{32a}$$

$$\text{s.t.} \quad \mathrm{PEB}\left(\{\delta_t \widehat{\mathbf{W}}_t\}_{t=1}^{N_t};\ \boldsymbol{\eta}(\mathbf{p}_u)\right) \leq \varrho,\ \forall \mathbf{p}_u \in \boldsymbol{\mathcal{U}}, \tag{32b}$$

$$(31b). \tag{32c}$$

To solve this semi-infinite optimization problem, we discretize $\boldsymbol{\mathcal{U}}$ into N_u points $\{\mathbf{p}_{u,i}\}_{i=1}^{N_u}$, and obtain the following approximated problem using Schur complement [43]:

$$\min_{\varrho, \{\delta_t\}_{t=1}^{N_t}, \{u_{i,m}\}_{i=1,m=1}^{N_u,3}} \quad \varrho \tag{33a}$$

$$\text{s.t.} \quad \begin{bmatrix} \mathbf{J}_{\boldsymbol{\eta}}\left(\{\delta_t \widehat{\mathbf{W}}_t\}_{t=1}^{N_t};\ \boldsymbol{\eta}(\mathbf{p}_{u,i})\right) & [\mathbf{I}_5]_{:,m} \\ [\mathbf{I}_5]_{:,m}^{\mathsf{T}} & u_{i,m} \end{bmatrix} \succeq 0, \tag{33b}$$

$$\sum_{m=1}^{3} u_{i,m} \leq \varrho, \tag{33c}$$

$$(31b),$$

$$m = 1, 2, 3,\ i = 1, \ldots, N_u.$$

From the proof of Lemma 1, each element of the FIM is an affine function of the codeword covariance matrices $\{\delta_t \widehat{\mathbf{W}}_t\}_{t=1}^{N_t}$. Hence, the constraint in (33b) is a linear matrix inequality (LMI) in the variables $\{\delta_t\}_{t=1}^{N_t}$ and $\{u_{i,m}\}$, and the power-allocation problem in (33) is a convex semidefinite program (SDP) [43] in the coefficients $\{\delta_t\}_{t=1}^{N_t}$. Consequently, it can be efficiently solved using convex optimization solvers.

D. Complexity of Power Optimization

According to [44, Ch. 11], [45], the SDP has the following complexity: $O\left(U^2 \sum_{i=1}^{K} n_i^2 + U \sum_{i=1}^{K} n_i^3\right)$, where U, K denote the number of optimization variables and the number of LMI constraints, respectively, and n_i is the row/column width of the i-th LMI matrix. In the SDP (31), we have $U = 3N_u + N_t + 1$ and $K = 3N_u$. Thus, assuming $N_u \gg N_t$, the complexity of (31) is approximately $O(N_u^3)$.

V. Hybrid Codebook Design: Finite State Selection Model

In this section, we investigate the same problem discussed in Sec. IV using the finite-state selection ER-FAS model explained in Sec. III-B. Under the perfect knowledge of the state parameters $\boldsymbol{\eta}$, the problem can be formulated as follows:

$$\min_{\{\overline{\mathbf{E}}_t\}_{t=1}^{N_t}, \{\mathbf{f}_t\}_{t=1}^{N_t}} \ \mathrm{PEB}\left(\{\overline{\mathbf{E}}_t\}_{t=1}^{N_t}, \{\mathbf{f}_t\}_{t=1}^{N_t};\ \boldsymbol{\eta}\right) \tag{34a}$$

$$\text{s.t.} \quad \|[\overline{\mathbf{E}}_t]_{m,[(m-1)Q+1:mQ]}\|_0 = 1, \tag{34b}$$

$$\overline{\mathbf{E}}_t \in \{0,1\}^{M\times MS}$$
$$\sum_{t=1}^{N_t} \mathbf{f}_t^{\mathsf{H}}\mathbf{f}_t = 1, \tag{34c}$$
$$m = 1,\ldots,M,\ t = 1,\ldots,N_t,$$

where the constraint (34b) is equivalent to unit norm constraint $\|\overline{\mathbf{e}}_{m,t}\|_0 = 1$ discussed in Sec. III-B, and (34c) is the power constraint. Problem (34) is non-convex with a large number of coupled discrete and continuous variables. To render (34) more tractable and simpler, similar to Sec. IV-A, we define the vectors $\{\overline{\mathbf{w}}_t\}_{t=1}^{N_t}$ as follows:

$$\overline{\mathbf{w}}_t = \overline{\mathbf{E}}_t^{\mathsf{T}}\mathbf{f}_t \in \mathbb{C}^{MS}. \tag{35}$$

In a similar manner to Sec. IV-A, the following equivalent problem can be obtained:

$$\min_{\overline{\mathbf{W}}} \quad \mathrm{PEB}\left(\overline{\mathbf{W}};\boldsymbol{\eta}\right) \tag{36a}$$
$$\text{s.t.} \quad \mathrm{tr}\left(\overline{\mathbf{W}}\right) = 1, \tag{36b}$$
$$\mathrm{rank}(\overline{\mathbf{W}}) \le N_t, \tag{36c}$$

where the power constraint is equivalent to (34c) [2], which can be transformed to a convex problem by dropping the rank constraint in (36c). Hence, due to an analogy between problems (25) and (36), for a given 2D-AOD $\boldsymbol{\theta}$, the following three codewords are sufficient to achieve the optimal value:

$$\widehat{\overline{\mathbf{w}}}_i = \sqrt{\delta_i}\frac{\overline{\mathbf{c}}^{(i)}(\boldsymbol{\theta})^*}{\|\overline{\mathbf{c}}^{(i)}(\boldsymbol{\theta})\|}, \tag{37}$$

where

$$\overline{\mathbf{c}}^{(1)}(\boldsymbol{\theta}) = \overline{\mathbf{c}}(\boldsymbol{\theta}),\ \overline{\mathbf{c}}^{(2)}(\boldsymbol{\theta}) = \frac{\partial\overline{\mathbf{c}}(\boldsymbol{\theta})}{\partial\theta^{\mathrm{el}}},\ \overline{\mathbf{c}}^{(3)}(\boldsymbol{\theta}) = \frac{\partial\overline{\mathbf{c}}(\boldsymbol{\theta})}{\partial\theta^{\mathrm{az}}}. \tag{38}$$

In (37), δ_1, δ_2, and δ_3 are power allocation coefficients. In the rest of the paper, we will refer to these three codewords by Type-1, Type-2, and Type-3 codewords, respectively, which depend on the 2D-AOD $\boldsymbol{\theta}$.

Although the three codewords in (37) achieve the optimum of (36), for a given state vector $\boldsymbol{\eta}$, the closed-from BB and EM precoders in (35) that satisfy these codewords cannot be found because of the ℓ_0-norm constraint in (34b) unique to the finite-state selection model. To address this, we employ an alternating-optimization procedure to construct admissible codewords $\widehat{\overline{\mathbf{w}}}_i$ whose beampatterns closely approximate those of the optimal vectors $\widehat{\overline{\mathbf{w}}}_i$. Specifically, we first derive a closed-form solution for the BB precoders with fixed EM precoders $\{\overline{\mathbf{E}}_i\}_{i=1}^3$, then optimize the EM precoders, and finally present a robust codebook design along with the optimization of power-allocation coefficients.

A. Baseband Precoders Design Under Fixed EM Precoders

In this subsection, we obtain a closed-form structure of the optimal BB precoders for fixed EM precoders $\{\overline{\mathbf{E}}_i\}_{i=1}^3$. With this assumption, the received interference-free signal at the t-th transmission, can be represented as follows:

$$\mathbf{y}_t = \sqrt{P}\,\alpha\,\mathbf{d}(\tau)\,\mathbf{q}_t(\boldsymbol{\theta})^{\mathsf{T}}\,\mathbf{f}_t \;+\; \mathbf{v}_t, \tag{39}$$

where $\mathbf{q}_t(\boldsymbol{\theta})$ only depends on $\boldsymbol{\theta}$ due to fixed EM precoders. Thus, the optimization problem *under fixed EM precoders* can be formulated as follows:

$$\min_{\{\mathbf{f}_t\}_{t=1}^{N_t}} \quad \mathrm{PEB}\left(\{\mathbf{f}_t\}_{t=1}^{N_t};\ \{\overline{\mathbf{E}}_t\}_{t=1}^{N_t},\boldsymbol{\eta}\right) \tag{40a}$$
$$\text{s.t.} \quad \text{(34c)}.$$

Proposition 3. *Assuming a perfect knowledge of UE position, and based on the optimal low-dimensional structure of the BB precoders under fixed EM precoders, we propose the following three BB precoders, which approximately achieve the optimum of* (40)*:*

$$\hat{\mathbf{f}}_i = \sqrt{\delta_i}\frac{\overline{\mathbf{E}}_i\overline{\mathbf{c}}^{(i)}(\boldsymbol{\theta})^*}{\|\overline{\mathbf{E}}_i\overline{\mathbf{c}}^{(i)}(\boldsymbol{\theta})\|}, \tag{41}$$

for $i = 1,2,3$, where δ_i is the proportion of the total power dedicated to the i-th codeword.

Proof. See Appendix D.

B. Proposed Heuristic Optimization for EM Precoders

In Prop. 3, we proposed three codewords for BB precoders under fixed EM precoders based on optimal low-dimensional solutions of (34). In this subsection, we investigate the optimization of the corresponding EM precoders $\{\overline{\mathbf{E}}_i\}_{i=1}^3$. By substituting the optimal structure of the BB precoders (41) into (35), we obtain the following simplified equation:

$$\overline{\mathbf{w}}_i(\overline{\mathbf{E}}_i,\boldsymbol{\theta}) = \sqrt{\delta_i}\frac{\overline{\mathbf{E}}_i^{\mathsf{T}}\overline{\mathbf{E}}_i\overline{\mathbf{c}}^{(i)}(\boldsymbol{\theta})^*}{\|\overline{\mathbf{E}}_i\overline{\mathbf{c}}^{(i)}(\boldsymbol{\theta})\|}, \tag{42}$$

for $i \in \{1,2,3\}$, where we have highlighted that the candidate vectors $\overline{\mathbf{w}}_i$ can be viewed as a function of $\overline{\mathbf{E}}_i,\boldsymbol{\theta}$.

For each $i \in \{1,2,3\}$, we optimize the EM precoding matrix $\overline{\mathbf{E}}_i$ so that the resulting beampattern of $\overline{\mathbf{w}}_i(\overline{\mathbf{E}}_i,\boldsymbol{\theta})$ best approximates the non-admissible optimal vector $\widehat{\overline{\mathbf{w}}}_i$ in (37). To this end, let $\boldsymbol{\Theta} \in \mathbb{R}^{N_g\times 2}$ be a discretized 2D-AOD grids of N_g angle pairs, and let $\overline{\mathbf{C}} \in \mathbb{C}^{MS\times N_g}$ collect the corresponding vectors $\overline{\mathbf{c}}(\boldsymbol{\theta}_n)$ at each grid point i.e., $\overline{\mathbf{C}} = [\overline{\mathbf{c}}(\boldsymbol{\theta}_1),\ldots,\overline{\mathbf{c}}(\boldsymbol{\theta}_{N_g})]$. The design of $\overline{\mathbf{E}}_i$, which depends on the true 2D-AOD $\boldsymbol{\theta}$, can then be cast as the following optimization problem:

$$\widehat{\overline{\mathbf{E}}}_i(\boldsymbol{\theta}) = \underset{\overline{\mathbf{E}}_i}{\mathrm{argmin}} \quad \|\overline{\mathbf{C}}^{\mathsf{T}}\overline{\mathbf{w}}_i(\overline{\mathbf{E}}_i,\boldsymbol{\theta}) - \overline{\mathbf{C}}^{\mathsf{T}}\widehat{\overline{\mathbf{w}}}_i\|^2, \tag{43}$$

where $\overline{\mathbf{C}}^{\mathsf{T}}\overline{\mathbf{w}}_i$ and $\overline{\mathbf{C}}^{\mathsf{T}}\widehat{\overline{\mathbf{w}}}_i$ are the beampatterns of $\overline{\mathbf{w}}_i$ and $\widehat{\overline{\mathbf{w}}}_i$ evaluated at the grids $\boldsymbol{\theta}_1,\ldots,\boldsymbol{\theta}_{N_g}$, respectively (see (17) and (35)). After substituting (37) and (42) into (43), the problem can be represented as:

$$\widehat{\overline{\mathbf{E}}}_i(\boldsymbol{\theta}) = \underset{\overline{\mathbf{E}}_i}{\mathrm{argmin}} \quad \underbrace{\left\|\frac{\overline{\mathbf{C}}^{\mathsf{T}}\overline{\mathbf{E}}_i^{\mathsf{T}}\overline{\mathbf{E}}_i\overline{\mathbf{c}}^{(i)}(\boldsymbol{\theta})^*}{\|\overline{\mathbf{E}}_i\overline{\mathbf{c}}^{(i)}(\boldsymbol{\theta})\|} - \frac{\overline{\mathbf{C}}^{\mathsf{T}}\overline{\mathbf{c}}^{(i)}(\boldsymbol{\theta})^*}{\|\overline{\mathbf{c}}^{(i)}(\boldsymbol{\theta})\|}\right\|^2}_{\mathcal{G}_i(\overline{\mathbf{E}}_i;\ \boldsymbol{\theta})}, \tag{44}$$

where we have dropped the power allocation coefficient δ_i as it does not affect the optimization.

Solving (44) by exhaustive search over all S^M combinations is computationally expensive when S or M is large. Thus, we adopt the BCD algorithm detailed in Algorithm 1. Specifically, we initialize the EM precoder $\overline{\mathbf{E}}_i$ and then, at each iteration, sequentially sweep through all M antennas. For each antenna, we select the pattern that minimizes the objective function while holding the others fixed. The algorithm terminates when either the absolute change in the objective between consecutive

[2]From (35), we have $\|\overline{\mathbf{w}}_t\| = \|\overline{\mathbf{E}}_t^{\mathsf{T}}\mathbf{f}_t\| = \|\mathbf{f}_t\|$. Hence, $\mathrm{tr}\left(\overline{\mathbf{W}}\right) = \sum_{t=1}^{N_t}\mathrm{tr}\left(\overline{\mathbf{W}}_t\right) = \sum_{t=1}^{N_t}\|\overline{\mathbf{w}}_t\|^2 = \sum_{t=1}^{N_t}\|\mathbf{f}_t\|^2 = 1$.

iterations falls below a threshold ϵ, or the iteration count exceeds $N_{\max}$.

Algorithm 1 Proposed BCD algorithm for EM precoder optimization

1: **Inputs**: Non-admissible optimal codeword $\widehat{\overline{\mathbf{w}}}_i$ defined in (37), 2D-AOD $\boldsymbol{\theta}$, matrix $\overline{\mathbf{C}}$, convergence threshold ϵ, max iterations $N_{\max}$.
2: **Output**: Optimal EM precoder matrix $\widehat{\overline{\mathbf{E}}}_i$
3: **Initialization**: Randomly initialize $\overline{\mathbf{E}}_i$, and set iteration number $r \leftarrow 0$. Moreover, set the initial objective function $\mathcal{G}_i^0$ using (44).
4: **while** $|\mathcal{G}_i^r - \mathcal{G}_i^{r-1}| > \epsilon$ or $r > N_{\max}$ **do**
5: **for** Antenna index $m = 1 : M$ **do**
6: Update the state of the m-th antenna to s, i.e., $[\overline{\mathbf{E}}_i]_{m,((m-1)S+s)} = 1$, which would achieve the lowest objective function $\mathcal{G}_i$ in (44).
7: **end for**
8: Increment iteration number: $r \leftarrow r + 1$.
9: Calculate the objective function $\mathcal{G}_i^r$ using (44).
10: **end while**

C. Proposed Codebook

Similar to Sec. IV-B, let $\{\boldsymbol{\theta}_\ell\}_{\ell=1}^L$ be L uniformly spaced AODs spanning the uncertainty region $\mathcal{U}$. Based on the optimal BB precoders in (41) and the optimal EM precoders in (44), we construct a codebook of $N_t = 3L$ codewords, comprising both BB and EM precoders, as follows:

$$\overline{\boldsymbol{\mathcal{E}}} = \left\{ \widehat{\overline{\mathbf{E}}}_1(\boldsymbol{\theta}_\ell), \widehat{\overline{\mathbf{E}}}_2(\boldsymbol{\theta}_\ell), \widehat{\overline{\mathbf{E}}}_3(\boldsymbol{\theta}_\ell) \right\}_{\ell=1}^{L}. \tag{45}$$

$$\overline{\boldsymbol{\mathcal{F}}} = \left\{ \sqrt{\delta_{3\ell-2}}\hat{\mathbf{f}}_1(\boldsymbol{\theta}_\ell), \sqrt{\delta_{3\ell-1}}\hat{\mathbf{f}}_2(\boldsymbol{\theta}_\ell), \sqrt{\delta_{3\ell}}\hat{\mathbf{f}}_3(\boldsymbol{\theta}_\ell) \right\}_{\ell=1}^{L},$$

The equivalent representation of this codebook based on optimized feasible vectors $\widetilde{\overline{\mathbf{w}}}_i(\boldsymbol{\theta}) = \overline{\mathbf{w}}_i(\widehat{\overline{\mathbf{E}}}_i, \boldsymbol{\theta})$ (obtained by substituting (44) into (42)) can be written as:

$$\overline{\boldsymbol{\mathcal{W}}} = \left\{ \sqrt{\delta_{3\ell-2}}\widetilde{\overline{\mathbf{w}}}_1(\boldsymbol{\theta}_\ell), \sqrt{\delta_{3\ell-1}}\widetilde{\overline{\mathbf{w}}}_2(\boldsymbol{\theta}_\ell), \sqrt{\delta_{3\ell}}\widetilde{\overline{\mathbf{w}}}_3(\boldsymbol{\theta}_\ell) \right\}_{\ell=1}^{L}. \tag{46}$$

In (45) and (46), we explicitly factor out the power-allocation coefficients to underscore that they are the only remaining optimization variables and to simplify the presentation of their optimization in the next subsection.

D. Power Allocation Optimization

The power allocation optimization problem given an uncertainty UE position region $\boldsymbol{\mathcal{U}}$ can be formulated as:

$$\min_{\{\delta_t\}_{t=1}^{N_t}} \max_{\boldsymbol{p}_u \in \boldsymbol{\mathcal{U}}} \quad \mathrm{PEB}\left(\{\delta_t \widetilde{\overline{\mathbf{W}}}_t\}_{t=1}^{N_t};\ \boldsymbol{\eta}(\mathbf{p}_u) \right) \tag{47a}$$

$$\text{s.t.} \quad \delta_t \geq 0,\ \sum_{t=1}^{N_t} \delta_t = 1, \tag{47b}$$

where $\delta_t \widetilde{\overline{\mathbf{W}}}_t = \delta_t \widetilde{\overline{\mathbf{w}}}_t \widetilde{\overline{\mathbf{w}}}_t^{\mathsf{H}}$ is the covariance matrix of the t-th codeword in (46). Problem (47) is similar to its counterpart for the synthesis scenario (31). Thus, this problem is also convex and the same methodologies explained in Sec. IV-C can be applied here.

E. Complexity of Algorithm 1

First, we obtain the complexity of evaluating $\mathcal{G}_i(\overline{\mathbf{E}}_i;\ \boldsymbol{\theta})$ in (44). Since the second term, i.e., $\overline{\mathbf{C}}^{\mathsf{T}}\overline{\mathbf{c}}^{(i)}(\boldsymbol{\theta})^*/\|\overline{\mathbf{c}}^{(i)}(\boldsymbol{\theta})\|$ does not depend on $\overline{\mathbf{E}}_i$, it is calculated once at the beginning of the algorithm with complexity $O(N_g MS)$. For the first term, we use the fact that $\overline{\mathbf{E}}_i^{\mathsf{T}}\overline{\mathbf{E}}_i = \mathrm{diag}(\widetilde{\mathbf{e}}_i)$, where $\widetilde{\mathbf{e}}_i = [\overline{\mathbf{e}}_{1,i}^{\mathsf{T}}, \ldots, \overline{\mathbf{e}}_{M,i}^{\mathsf{T}}]^{\mathsf{T}} \in \{0,1\}^{MS}$. Thus, $\overline{\mathbf{E}}_i^{\mathsf{T}}\overline{\mathbf{E}}_i\overline{\mathbf{c}}^{(i)}(\boldsymbol{\theta})^* = \widetilde{\mathbf{e}}_i \odot \overline{\mathbf{c}}^{(i)}(\boldsymbol{\theta})^*$. Hence, updating the m-th antenna state i.e., modifying $\overline{\mathbf{e}}_{m,i}$, requires the complexity of $O(N_g)$ to update the first term of $\mathcal{G}_i(\overline{\mathbf{E}}_i;\boldsymbol{\theta})$. Consequently, line 6 of Algorithm 1, which evaluates all S candidate states for antenna m, incurs $O(SN_g)$ complexity. Sweeping over M antennas in line 5 therefore costs $O(MSN_g)$ per iteration. Over a maximum of $N_{\max}$ iterations, optimizing one codeword has complexity $O(N_{\max}MSN_g)$, and executing the algorithm for all N_t codewords yields a total complexity of $O(N_t N_{\max} MSN_g)$.

Remark 3. *The codebooks in* (29) *and* (45) *can be constructed entirely offline. Concretely, for each 2D-AOD inside the uncertainty region, we precompute the corresponding BB and EM codewords on a discretized angular grid with $\theta^{\mathrm{az}} \in [-\pi, \pi)$ and $\theta^{\mathrm{el}} \in [0, \pi]$ at a chosen resolution. In online scenario, the BS then selects the precomputed entries that cover the given uncertainty region, avoiding costly real-time optimization and enabling low-latency deployment.*

VI. Maximum Likelihood Localization

Due to the analogy between the received signals between the two considered reconfigurability paradigms in (12) and (17), we only explain it for the synthesis scenario. The same methodology can be applied to finite-state selection model. The proposed approach consists of two steps: coarse positioning and refinement step, as detailed next.

A. Step 1: Coarse Positioning

1) Coarse Delay Estimation: After substituting (23) in (12), the received signal vector at the t-th transmission can be represented as:

$$\mathbf{y}_t = \beta_t\, \mathbf{d}(\tau) + \widetilde{\mathbf{v}}_t, \qquad t = 1, \ldots, N_t, \tag{48}$$

where τ and $\beta_t = \sqrt{P}\,\alpha\, \mathbf{c}(\boldsymbol{\theta})^{\mathsf{T}}\, \mathbf{w}_t \in \mathbb{C}$ are the delay and unknown complex gain of the LoS path, and $\widetilde{\mathbf{v}}_t \in \mathbb{C}^{N_s}$ denotes the joint contribution of the noise and interference. The estimation problem can be formulated as follows:

$$(\hat{\tau}, \{\hat{\beta}_t\}_{t=1}^{N_t}) = \underset{\tau, \{\beta_t\}_{t=1}^{N_t}}{\mathrm{argmin}} \sum_{t=1}^{N_t} \|\mathbf{y}_t - \beta_t \mathbf{d}(\tau)\|^2. \tag{49}$$

For a given fixed delay τ, the ML i.e., the least-squares (LS) estimate of β_t is obtained in closed form as:

$$\hat{\beta}_t(\tau) = \frac{\mathbf{d}(\tau)^{\mathsf{H}}\mathbf{y}_t}{\|\mathbf{d}(\tau)\|^2} = \frac{1}{N_s}\, \mathbf{d}(\tau)^{\mathsf{H}}\mathbf{y}_t, \tag{50}$$

where we used the fact that $\mathbf{d}(\tau)^{\mathsf{H}}\mathbf{d}(\tau) = N_s$. Substituting (50) into (49) and simplifying yields the following simplified delay estimation problem:

$$\hat{\tau} = \underset{\tau \in [\tau_{\min}, \tau_{\max}]}{\mathrm{argmin}} \sum_{t=1}^{N_t} |\mathbf{d}(\tau)^{\mathsf{H}}\mathbf{y}_t|^2 = \|\mathbf{d}(\tau)^{\mathsf{H}}\mathbf{Y}\|^2, \tag{51}$$

where $\mathbf{Y} = [\mathbf{y}_1, \ldots, \mathbf{y}_{N_t}]$, and $\tau_{\min}, \tau_{\max}$ are the minimum and maximum possible delays of the LoS path inside the uncertainty region $\boldsymbol{\mathcal{U}}$. Problem (51), can be solved by performing a simple linear search over N_τ uniformly spaced grids in the in the interval $[\tau_{\min}, \tau_{\max}]$.

2) Coarse AOD Estimation: After substituting the coarse delay estimate $\hat{\tau}$ and (48) back into (50):

$$\hat{\beta}_t = \frac{\mathbf{d}(\hat{\tau})^{\mathsf{H}}\mathbf{y}_t}{N_s} = \underbrace{\frac{\sqrt{P}\,\alpha\,\mathbf{d}(\hat{\tau})^{\mathsf{H}}\mathbf{d}(\tau)}{N_s}}_{\kappa}\,\mathbf{c}(\boldsymbol{\theta})^{\mathsf{T}}\mathbf{w}_t + \underbrace{\frac{\mathbf{d}(\hat{\tau})^{\mathsf{H}}\widetilde{\mathbf{v}}_t}{N_s}}_{n_t}, \tag{52}$$

where κ is an unknown scalar, and n_t is the resulted noise scalar after delay beamforming. Thus, after collecting the scalars $\hat{\beta}_t$ into a vector $\hat{\boldsymbol{\beta}} = [\hat{\beta}_1, \ldots, \hat{\beta}_{N_t}]^{\mathsf{T}}$, the estimation problem for $\boldsymbol{\theta}, \kappa$ can be formulated as follows:

$$(\hat{\boldsymbol{\theta}}, \hat{\kappa}) = \underset{\boldsymbol{\theta},\ \kappa}{\operatorname{argmin}} \|\hat{\boldsymbol{\beta}} - \kappa\,\mathbf{s}(\boldsymbol{\theta})\|^2\,, \tag{53}$$

where $\mathbf{s}(\boldsymbol{\theta}) = \mathbf{c}(\boldsymbol{\theta})^{\mathsf{T}}\mathbf{W}$ and $\mathbf{W} = [\mathbf{w}_1, \ldots, \mathbf{w}_{N_t}]$. For fixed $\boldsymbol{\theta}$, the closed form LS estimate of κ is obtained as: $\hat{\kappa}(\boldsymbol{\theta}) = \frac{\mathbf{s}(\boldsymbol{\theta})^{\mathsf{H}}\hat{\boldsymbol{\beta}}}{\|\mathbf{s}(\boldsymbol{\theta})\|^2}$. Substituting $\hat{\kappa}(\boldsymbol{\theta})$ into (53) and simplifying yields the following simplified 2D-AOD estimation problem:

$$\hat{\boldsymbol{\theta}} = \underset{\boldsymbol{\theta}}{\operatorname{argmin}} \frac{|\mathbf{s}(\boldsymbol{\theta})^{\mathsf{H}}\hat{\boldsymbol{\beta}}|^2}{\|\mathbf{s}(\boldsymbol{\theta})\|^2}\,, \tag{54}$$

which can be solved via a simple 2D search over N_θ AOD grids inside uncertainty region $\boldsymbol{\mathcal{U}}$.

Hence, combining the coarse delay and 2D-AOD estimates $\hat{\tau}$ and $\hat{\boldsymbol{\theta}}$, the coarse estimate of the UE position is obtained as: $\tilde{\boldsymbol{p}}_u = c\,\hat{\tau}\,\hat{\mathbf{u}}$, $\hat{\mathbf{p}}_u = \boldsymbol{R}\,\tilde{\boldsymbol{p}}_u + \boldsymbol{p}_b$, where $\hat{\boldsymbol{u}}$ is the unit direction towards the estimated 2D-AOD $\hat{\boldsymbol{\theta}}$, and $\tilde{\boldsymbol{p}}_u$ denotes the estimated position in the local coordinates of the ER-FAS, and finally $\hat{\boldsymbol{p}}_u$ is the estimated UE position in the global coordinates.

B. Step 2: Position Refinement

For the refinement step, we consider direct localization. In particular, the estimation problem can be formulated as:

$$(\hat{\zeta},\ \hat{\mathbf{p}}_u) = \underset{\zeta,\ \mathbf{p}}{\operatorname{argmin}} \quad \sum_{t=1}^{N_t} \|\mathbf{y}_t - \zeta\mathbf{x}_t\|^2, \tag{55}$$

where $\zeta = \sqrt{P}\,\alpha$ is the unknown overall complex gain and $\mathbf{x}_t = \mathbf{d}(\tau)\,\mathbf{c}(\boldsymbol{\theta})^{\mathsf{T}}\mathbf{w}_t$. It is easy to observe that the ML estimate of ζ minimizing (55) is obtained as: $\hat{\beta}(\mathbf{p}_u) = \frac{\widetilde{\mathbf{x}}^{\mathsf{H}}\widetilde{\mathbf{y}}}{\|\widetilde{\mathbf{x}}\|^2}$, where $\widetilde{\mathbf{x}} = [\mathbf{x}_1^{\mathsf{T}}, \ldots, \mathbf{x}_{N_t}^{\mathsf{T}}]^{\mathsf{T}}$, and $\widetilde{\mathbf{y}} = [\mathbf{y}_1^{\mathsf{T}}, \ldots, \mathbf{y}_{N_t}^{\mathsf{T}}]^{\mathsf{T}}$. After substituting $\hat{\beta}(\mathbf{p}_u)$ back into (55), the direct localization problem can be simplified as:

$$\hat{\mathbf{p}}_u = \underset{\mathbf{p}_u}{\operatorname{argmin}} \quad \frac{|\widetilde{\mathbf{x}}^{\mathsf{H}}\widetilde{\mathbf{y}}|^2}{\|\widetilde{\mathbf{x}}\|^2}\,. \tag{56}$$

Utilizing the initial position estimate in the previous subsection, we apply the derivative-free Nelder-Mead (NM) algorithm [46], [47] to iteratively refine the UE position. In particular, starting with the initial estimate $\hat{\mathbf{p}}_u$ in the previous subsection, this fast simplex-based algorithm searches $\mathcal{U}$ in an off-grid manner, leading to an accurate position estimate.

C. Complexity of the Proposed Localization Method

The delay estimation problem (51) has the complexity $O(N_s N_t N_\tau)$, the complexity of AOA estimation in (54) is $O(N_t N_\theta)$. The computation of the objective function (56) has the complexity $O(N_t N_s M Q)$. Thus, the complexity of the second step, i.e., the position refinement, is given by $O(N_{\text{nm}} N_t N_s M Q)$, where N_{nm} is the average number of iterations in the NM algorithm until convergence.

VII. Simulations

In this section, we evaluate the performance of the proposed codebook design and localization for ER-FAS-assisted mmWave systems through numerical simulations.

A. Simulation Setup

The scenario under consideration includes a BS equipped with a UPA with the same number of rows and columns $M^h = M^v$, and a single UE. The default system parameters are presented in Table I. Note that some parameters may vary in different simulations. According to the selected uncertainty region $\mathcal{U}$ in Table I, the elevation and azimuth intervals are uniformly sampled with a grid step of $d_\theta = d_\phi = \frac{1.8}{M^h}\,\text{rad}$ from which the values of L and N_t are determined[3]. For instance, for $M^h = M^v = 5$, $d_\theta = d_\phi \approx 20.63^\circ$ resulting in $L = 3$ 2D-AODs and $N_t = 3L = 9$ codewords. In the finite-state selection model, we utilize $N_g = 1000$ angular grid points to optimize each EM precoder in solving (43). The channel amplitudes are modeled according to the well-known free-space path loss model $\rho = \frac{\lambda}{4\pi\|\mathbf{p}_b - \mathbf{p}_u\|}$ for the LoS path and $\rho_i = \frac{\sqrt{4\pi s_i}\lambda}{16\pi^2\|\mathbf{p}_b - \mathbf{p}_s^{(i)}\|\|\mathbf{p}_s^{(i)} - \mathbf{p}_u\|}$ for the i-th MPC. The phase components are generated uniformly from the interval $[-\pi, \pi]$. The transmit power P is varied to obtain different received SNR levels on the LoS path, defined as $\text{SNR} = \frac{P\rho^2}{N_0 B}$ [41], where N_0 is the noise power spectral density, and B is the bandwidth. We use RMSE and PEB metrics to evaluate the performance of the proposed methods. Each RMSE value is estimated using 1000 Monte-Carlo trials. In all simulations, optimal power allocation is used unless stated otherwise. Moreover, except for the simulations reported in Sec. VII-F, we assume an interference-free environment.

TABLE I: System parameters

Default System Parameters and Symbol	**Value**
Carrier frequency f_c	$30\,\text{GHz}$
Noise PSD N_0	$-173.855\,\text{dBm}$
Light speed c	$3 \times 10^8\,\text{m/s}$
Subcarrier spacing Δf	$200\,\text{kHz}$
Bandwidth B	$100\,\text{MHz}$
UE position $\mathbf{p}_u$	$[45, 5, 2]^{\mathsf{T}}$
Number of SHOD bases Q	4
Uncertainty region $\mathcal{U}$	$30 < x < 50, -10 < y < 10,\ 0 < z < 10$
Elevation Angle Bounds $[\theta^{\text{el}}_{\min}, \theta^{\text{el}}_{\max}]$	$[80.53^\circ, 99.46^\circ]$
Azimuth Angle Bounds $[\theta^{\text{az}}_{\min}, \theta^{\text{az}}_{\max}]$	$[-18.43^\circ, 18.43^\circ]$
BS position $\mathbf{p}_b$	$[0, 0, 5]^{\mathsf{T}}\,[\text{m}]$
BS number of elements M^h, M^v	5, 5
Localization parameters N_τ, N_θ	1000, 500

B. Beampattern Analysis

In our first simulation, we compare the beampatterns of a representative codeword from our proposed synthesis codebook (29) and finite-state selection codebook (45), both evaluated at $\boldsymbol{\theta} = [90^\circ, 0^\circ]^{\mathsf{T}}$. The beampatterns are shown for all three types of codewords in Fig. 2. Here, we denote the

[3]These values are set according to the half-power beamwidth of the BS.

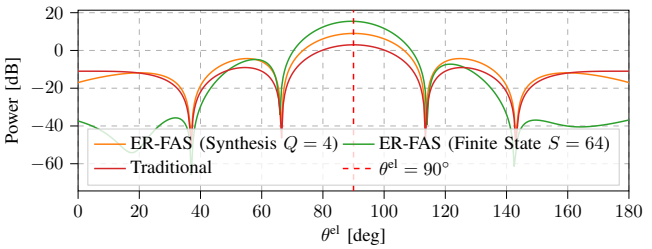

(a) 1D beampattern of Type-1 codeword for fixed $\theta^{\text{az}} = 0°$

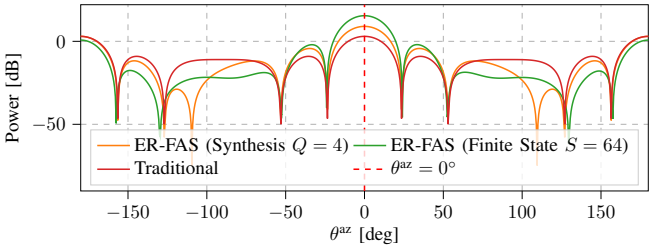

(b) 1D beampattern of Type-1 codeword for fixed $\theta^{\text{el}} = 90°$

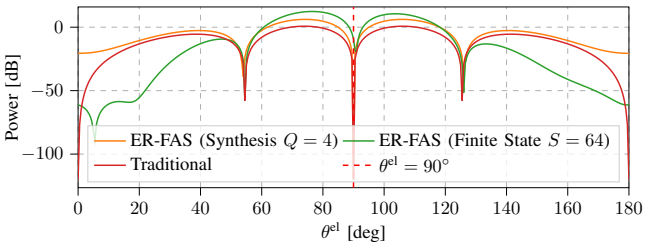

(c) 1D beampattern of Type-2 codeword for fixed $\theta^{\text{az}} = 0°$

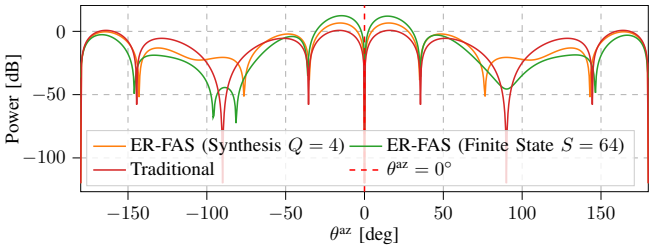

(d) 1D Beampattern of Type-3 codeword at $\theta^{\text{el}} = 90°$, $Q = 64$

Fig. 2: 1D beampatterns of the optimized codeword.

beampattern for the synthesis model by $p(\boldsymbol{\theta}^*)$ and for the finite-state model by $\overline{p}(\boldsymbol{\theta}^*)$, which are defined as:

$$p(\boldsymbol{\theta}^*) = \frac{|\mathbf{c}(\boldsymbol{\theta}^*)^{\mathsf{T}}\mathbf{w}|^2}{\|\mathbf{w}\|^2}, \ \overline{p}(\boldsymbol{\theta}^*) = \frac{|\overline{\mathbf{c}}(\boldsymbol{\theta}^*)^{\mathsf{T}}\overline{\mathbf{w}}|^2}{\|\overline{\mathbf{w}}\|^2}. \quad (57)$$

where $\boldsymbol{\theta}^*$ is an arbitrary 2D-AOD grid. From Figs. 2a and 2b, the ER-FAS achieves approximately $13.98\,\text{dB}$ higher peak beampattern gain than the traditional non-reconfigurable array for $S = 64$ in finite-state selection model. Similarly, the peak of the beampattern using ER-FAS with $Q = 4$ in the synthesis model is $6\,\text{dB}$ above the traditional array.

C. Performance Under Different Power Allocation Schemes

In this subsection, we assess the performance of the optimal power allocation of the codewords proposed in Sec. IV-C and Sec. V-D. The uniform power allocation scheme is used as a baseline for comparative analysis. It is noteworthy that the uniform power allocation is a common heuristic approach in the state-of-the-art approaches [6], [38] using traditional arrays. To this end, we obtain the PEB values for different UE positions inside a square within $x \in [30, 50]$ and $y \in [-10, 10]$ at a fixed height $z = 2$ and fixed $\text{SNR} = 5\,\text{dB}$. As shown in Fig. 3, the proposed optimized power allocation consistently outperforms the uniform power allocation strategy, demonstrating its effectiveness.

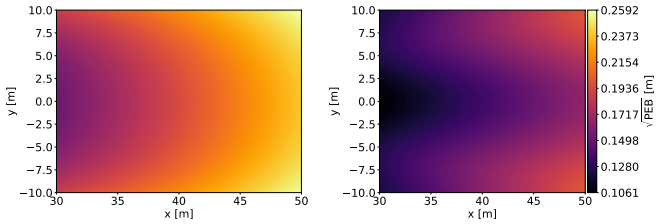

(a) Uniform power allocation (b) Optimal power allocation

Fig. 3: Evaluation of the proposed power allocation.

D. Localization Performance Versus SNR

In Fig. 4, the RMSE and corresponding PEB of the proposed ML-based localization from Sec. VI are plotted for three array configurations: the ER-FAS under the synthesis model with $Q = 4$ SHOD bases, the ER-FAS under the finite-state selection model with $S = 64$, and a traditional non-reconfigurable array employing the optimal codebooks proposed in [41], [45]. It is shown that both ER-FAS configurations substantially outperform the traditional array in localization accuracy. Moreover, the ER-FAS is more robust than a traditional array in low-SNR regimes.

E. Impact of the Number of Bases and States

Figs. 5 and 6 plot the PEB of the proposed method under the synthesis and finite-state selection models versus the number of SHOD bases Q and states S, respectively, for various antenna geometries. The optimized traditional non-reconfigurable array is used as a baseline. As expected, the performance of the proposed method improves with increasing Q or S. However, the traditional array is fixed as it does not depend on either Q or S. Additionally, Fig. 5 shows that the optimal traditional array coincides with the ER-FAS synthesis design when $Q = 1$. This equivalence follows because the first SHOD basis is constant on the unit sphere. Consequently, the synthesis construction with $Q = 1$ reduces to the optimal traditional array. See Appendix A-B for proof. Moreover, Fig. 6 shows that a 5×5 UPA ER-FAS outperforms a traditional 10×10 UPA for $S \geq 19$, achieving equivalent localization accuracy with significantly fewer elements, thereby simplifying practical deployment. Analogous observations hold for other array geometries.

F. Localization Performance Under Interference

In this subsection, we evaluate the robustness of the proposed methods in the presence of interference. We also consider the traditional non-reconfigurable array as a baseline. To this end, we consider $I = 40$ MPCs to model interference. The positions of these MPCs are randomly generated inside the UE uncertainty region $\boldsymbol{\mathcal{U}}$. Then, we obtain the RMSE and PEB metrics versus line-of-sight to multipath ratio (LMR) [38, Eq. (24)] at a fixed $\text{SNR} = 0\,\text{dB}$ in the interval $\text{LMR} \in [0\,\text{dB}, 45\,\text{dB}]$ as shown in Fig. 7. Each RMSE value is computed using 1000 Monte-Carlo trials. As discussed in Sec. III-C1, since the FIM analysis in this paper considers

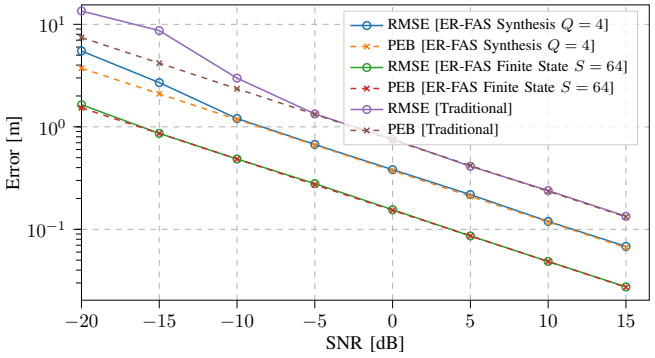

Fig. 4: Localization performance versus SNR.

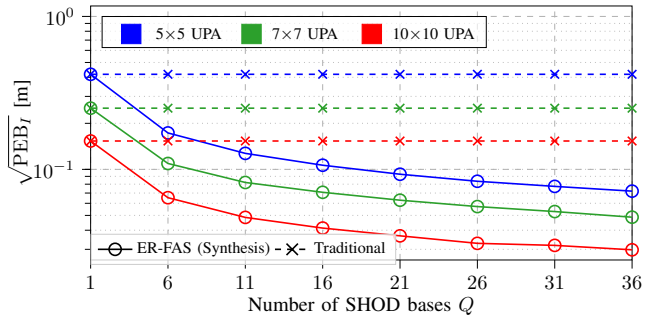

Fig. 5: Localization performance versus number of SHOD bases.

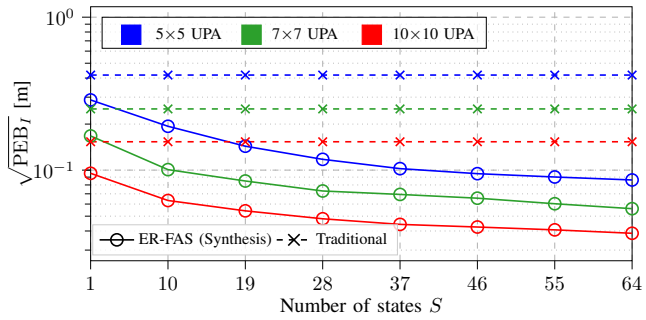

Fig. 6: Localization performance versus number of states.

only LoS path, the PEB is fixed for each LMR. However, RMSE converge to the PEB at approximately $\text{LMR} = 15\,\text{dB}$, and the proposed ER-FAS is close to the PEB in $\text{LMR} \in [10\,\text{dB}, 15\,\text{dB}]$. It is evident that the proposed method using ER-FAS substantially outperforms the traditional non-reconfigurable array even in challenging low-LMR regimes. The performance degradation in low LMR is due to the strong multipath components and weak LoS path, resulting a model mismatch thereby degrading the localization performance. However, it is noteworthy that based on mmWave channel measurements, the power of the LoS component is shown to be around $13\,\text{dB}$ greater than that of the NLoS components [48], [49]. Thus, the proposed method remains robust in practical scenarios.

VIII. Conclusion

In this paper, we investigated the joint design of BB and EM precoders to maximize downlink localization accuracy in an ER-FAS-enabled MISO system. We considered two reconfigurability paradigms: (i) a synthesis model, where each antenna synthesizes beampatterns from a set of orthonormal

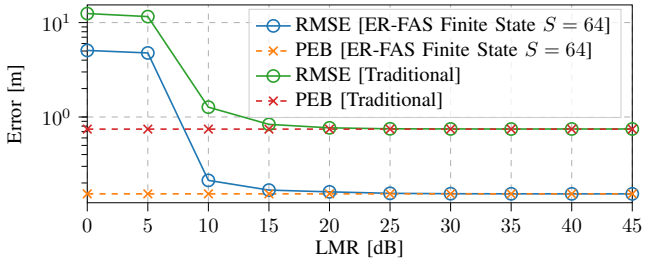

Fig. 7: Localization performance versus LMR.

basis functions, and (ii) a finite-state selection model, where each antenna chooses from a library of predefined patterns. For both paradigms, we proposed low-complexity codebooks for the BB and EM designs. For the finite-state model, we developed an efficient BCD algorithm to optimize the EM precoders. We complemented our designs with an efficient ML-based localization algorithm and extensive simulations, demonstrating substantial PEB and RMSE gains over traditional non-reconfigurable arrays. Future work will extend these methods to ISAC systems and assess robustness to model mismatch and hardware impairments.

Appendix A
Complex Spherical Harmonic Orthogonal Decomposition

SHOD bases represent any square-integrable function on the unit sphere as a weighted sum of orthonormal basis functions [39]. In antenna and array processing, SHOD provides a compact way to model 3D radiation patterns. Each basis function is indexed by a nonnegative integer degree ℓ and an integer order m with $-\ell \le m \le \ell$. The degree ℓ controls the overall spatial frequency (number of lobes), while the order m governs azimuthal variation. Low degrees (e.g. $\ell = 0$ or $\ell = 1$) yield broad, smooth patterns; higher ℓ produce finer angular structure and more nulls.

A. Definition of the Complex SHOD Bases

The complex spherical harmonics are defined for each degree $\ell \ge 0$ and order $-\ell \le m \le \ell$ by

$$Y_\ell^m(\theta^{\text{el}}, \theta^{\text{az}}) = (-1)^m \, N_{\ell m} \, P_\ell^m(\cos\theta^{\text{el}}) \, e^{\,jm\theta^{\text{az}}}, \tag{58}$$

where the normalization constant is $N_{\ell m} = \sqrt{\frac{2\ell+1}{4\pi} \frac{(\ell-m)!}{(\ell+m)!}}$, and $P_\ell^m(x)$ denotes the associated Legendre function. These functions satisfy the orthonormality relation

$$\int_{-\pi}^{\pi}\int_{0}^{\pi} Y_\ell^m(\theta^{\text{el}}, \theta^{\text{az}}) \left(Y_{\ell'}^{m'}(\theta^{\text{el}}, \theta^{\text{az}})\right)^* \times \sin\theta^{\text{el}} \, d\theta^{\text{el}} \, d\theta^{\text{az}} = \delta_{\ell\ell'} \, \delta_{mm'}, \tag{59}$$

where δ_{pq} is the Kronecker delta, equal to 1 if $p = q$ and 0 otherwise. To form a truncated dictionary of size Q, we select the first Q pairs (ℓ, m) in the ordering $(\ell, m) = (0,0), (1,-1), (1,0), (1,1), (2,-2), \ldots$ and denote the k-th base by $Y_k(\theta^{\text{el}}, \theta^{\text{az}})$.

B. Special Case: Recovering the Omni-Directional Pattern

The degree-zero spherical harmonic is $Y_0^0(\boldsymbol{\theta}) = N_{0,0} \, P_0^0(\cos\theta^{\text{el}}) = \sqrt{\frac{1}{4\pi}}$, a constant over the sphere. Hence, by choosing the EM precoder vector $\mathbf{e} = \left[1, 0, \ldots, 0\right]^{\mathsf{T}}$, so that $g(\boldsymbol{\theta}) = \mathbf{e}^{\mathsf{H}}\mathbf{b}(\boldsymbol{\theta}) = Y_0^0(\boldsymbol{\theta}) = \frac{1}{\sqrt{4\pi}}$, we can recover an *omni-directional* element radiation pattern.

C. Total Radiated Power Conservation

Consider the full 2D angular domain $\boldsymbol{\theta} = [\theta^{\text{el}}, \theta^{\text{az}}]^{\mathsf{T}}$ with $\theta^{\text{el}} \in [0, \pi]$, $\theta^{\text{az}} \in [-\pi, \pi)$.

1) Case 1: Synthesis Model: Since the bases $\mathbf{b}(\boldsymbol{\theta})$ are orthonormal over the sphere,

$$\int_0^{2\pi}\int_0^{\pi} \mathbf{b}(\boldsymbol{\theta})\,\mathbf{b}(\boldsymbol{\theta})^H \,\sin\theta^{\text{el}}\,d\theta^{\text{el}}\,d\theta^{\text{az}} \;=\; \mathbf{I}_Q, \tag{60}$$

Then, the total radiated power from an arbitrary antenna with a unit norm EM vector $\mathbf{e}$ can be calculated as:

$$\begin{aligned}&\int_0^{2\pi}\int_0^{\pi} |\mathbf{e}^{\mathsf{H}}\mathbf{b}(\boldsymbol{\theta})|^2 \sin\theta^{\text{el}}\,d\theta^{\text{el}}\,d\theta^{\text{az}}\\ &= \int_0^{2\pi}\int_0^{\pi} \mathbf{e}^{\mathsf{H}}\big[\mathbf{b}(\boldsymbol{\theta})b(\boldsymbol{\theta})^H\big]\mathbf{e}\sin\theta^{\text{el}}\,d\theta^{\text{el}}\,d\theta^{\text{az}}\\ &= \mathbf{e}^{\mathsf{H}}\Big[\int_0^{2\pi}\int_0^{\pi} \mathbf{b}\,\mathbf{b}^{\mathsf{H}}\,\sin\theta^{\text{el}}\,d\theta^{\text{el}}\,d\theta^{\text{az}}\Big]\mathbf{e} = \mathbf{e}^{\mathsf{H}}\mathbf{I}_Q\mathbf{e} = 1.\end{aligned}$$

2) Case 2: Finite-State Selection Model: Since $\|\overline{\mathbf{e}}_{m,t}\|_0 = 1$, we have $\big[\mathbf{g}_t(\boldsymbol{\theta})\big]_m = \overline{\mathbf{e}}_{m,t}^{\mathsf{T}}\,\overline{\mathbf{b}}(\boldsymbol{\theta}) = \overline{b}_s(\boldsymbol{\theta})$ for some $s \in \{1,\ldots,S\}$. Thus:

$$\begin{aligned}&\int_0^{2\pi}\int_0^{\pi} \big|\big[\mathbf{g}_t(\boldsymbol{\theta})\big]_m\big|^2 \sin\theta^{\text{el}}\,d\theta^{\text{el}}\,d\theta^{\text{az}}\\ &\qquad= \int_0^{2\pi}\int_0^{\pi} |\overline{b}_s(\boldsymbol{\theta})|^2 \sin\theta^{\text{el}}\,d\theta^{\text{el}}\,d\theta^{\text{az}} = 1.\end{aligned} \tag{61}$$

In both models the total radiated power over the full sphere remains 1, confirming the energy conservation law [3].

Appendix B
Proof of Prop. 1

Inspired by [50], $\mathbf{W} \succeq 0$ can be represented as:

$$\mathbf{W} = \mathbf{Q}\mathbf{Q}^{\mathsf{H}}. \tag{62}$$

Next, we decompose $\mathbf{Q}$ as $\mathbf{Q} = \boldsymbol{\Pi}_{\mathbf{C}_w}\mathbf{Q} + \boldsymbol{\Pi}^{\perp}_{\mathbf{C}_w}\mathbf{Q}$, and substitute it to (62) to obtain the following decomposition for $\mathbf{W}$:

$$\mathbf{W} = \boldsymbol{\Pi}_{\mathbf{C}_w}\mathbf{Q}\mathbf{Q}^{\mathsf{H}}\boldsymbol{\Pi}_{\mathbf{C}_w} + \widetilde{\mathbf{W}}, \tag{63}$$

where

$$\widetilde{\mathbf{W}} = \boldsymbol{\Pi}^{\perp}_{\mathbf{C}_w}\mathbf{Q}\mathbf{Q}^{\mathsf{H}}\boldsymbol{\Pi}^{\perp}_{\mathbf{C}_w} + \boldsymbol{\Pi}_{\mathbf{C}_w}\mathbf{Q}\mathbf{Q}^{\mathsf{H}}\boldsymbol{\Pi}^{\perp}_{\mathbf{C}_w} + \boldsymbol{\Pi}^{\perp}_{\mathbf{C}_w}\mathbf{Q}\mathbf{Q}^{\mathsf{H}}\boldsymbol{\Pi}_{\mathbf{C}_w}. \tag{64}$$

It can be easily verified that

$$\mathbf{C}_w^{\mathsf{H}}\widetilde{\mathbf{W}}\mathbf{C}_w = 0. \tag{65}$$

On the other hand, according to Lemma 1, the FIM elements only depend on the elements of the matrix $\mathbf{C}_w^{\mathsf{H}}\mathbf{W}\mathbf{C}_w \in \mathbb{C}^{3\times 3}$. Hence, according to (63) and (65), FIM does not depend on the component $\widetilde{\mathbf{W}}$ of $\mathbf{W}$. Moreover, from (64):

$$\text{tr}(\widetilde{\mathbf{W}}) = \text{tr}(\boldsymbol{\Pi}^{\perp}_{\mathbf{C}_w}\mathbf{Q}\mathbf{Q}^{\mathsf{H}}\boldsymbol{\Pi}^{\perp}_{\mathbf{C}_w}) = \|\mathbf{Q}^{\mathsf{H}}\boldsymbol{\Pi}^{\perp}_{\mathbf{C}_w}\|_{\text{F}}^2 \geq 0. \tag{66}$$

Thus, we conclude that $\widetilde{\mathbf{W}}$ is a component of $\mathbf{W}$ for which the FIM (and hence PEB) is not dependent on, and moreover, it contains nonnegative portion of the total transmitted power. Thus, for optimal solution $\mathbf{W}$ we must have $\text{tr}(\widetilde{\mathbf{W}}) = 0$ or equivalently $\mathbf{Q}^{\mathsf{H}}\boldsymbol{\Pi}^{\perp}_{\mathbf{C}_w} = 0$ from (66). Because otherwise, one can find a better solution by considering $\widetilde{\mathbf{W}} = 0$ (or equivalently reducing the power of $\widetilde{\mathbf{W}}$ to zero) and scaling the power of the first component of $\mathbf{W}$ in (63), which would yield a better solution with lower PEB. Hence, we conclude that an optimal solution $\mathbf{W}$ can be represented as follows:

$$\begin{aligned}\mathbf{W} &= \boldsymbol{\Pi}_{\mathbf{C}_w}\mathbf{Q}\mathbf{Q}^{\mathsf{H}}\boldsymbol{\Pi}_{\mathbf{C}_w}\\ &= \mathbf{C}_w\underbrace{(\mathbf{C}_w^{\mathsf{H}}\mathbf{C}_w)^{-1}\mathbf{C}_w^{\mathsf{H}}\mathbf{Q}\mathbf{Q}^{\mathsf{H}}\mathbf{C}_w(\mathbf{C}_w^{\mathsf{H}}\mathbf{C}_w)^{-1}}_{\stackrel{\text{def}}{=}\boldsymbol{\Xi}}\mathbf{C}_w^{\mathsf{H}}\\ &= \mathbf{C}_w\boldsymbol{\Xi}\mathbf{C}_w^{\mathsf{H}},\end{aligned} \tag{67}$$

where $\boldsymbol{\Xi} \in \mathbb{C}^{3\times 3}$ and $\boldsymbol{\Xi} \succeq 0$, which completes the proof.

Appendix C
Proof of Prop. 2

According to Prop. 1:

$$\begin{aligned}\mathbf{W} &= \sum_{t=1}^{N_t}\mathbf{W}_t = \sum_{t=1}^{N_t}\mathbf{w}_t\mathbf{w}_t^{\mathsf{H}}\\ &= \mathbf{C}_w\boldsymbol{\Xi}\mathbf{C}_w^{\mathsf{H}} = \sum_{i=1}^{3}\sum_{j=1}^{3}[\boldsymbol{\Xi}]_{i,j}[\mathbf{C}_w]_{:,i}[\mathbf{C}_w]_{:,j}^{\mathsf{H}}.\end{aligned} \tag{68}$$

Thus, we should first optimize the elements of the matrix $\boldsymbol{\Xi}$ to minimize the objective function (25), and then find suitable parameter N_t and vectors $\{\mathbf{w}_t\}_{t=1}^{N_t}$ to satisfy (68). Observing (68), in order to make the problem easier and more tractable, we relax the problem by restricting $\boldsymbol{\Xi}$ to be a diagonal matrix $\boldsymbol{\Xi} = \text{diag}(\boldsymbol{\xi})$ for some vector $\boldsymbol{\xi} \in \mathbb{R}_+^3$ with nonnegative elements. After substituting this equation in (68):

$$\sum_{t=1}^{N_t}\mathbf{w}_t\mathbf{w}_t^{\mathsf{H}} = \sum_{i=1}^{3}[\xi]_i[\mathbf{C}_w]_{:,i}[\mathbf{C}_w]_{:,i}^{\mathsf{H}}, \tag{69}$$

which admits the following closed-form solutions:

$$N_t = 3,\ \mathbf{w}_i = \sqrt{[\xi]_i}[\mathbf{C}_w]_{:,i}, \tag{70}$$

for $i = 1, 2, 3$. It is easy to see that $[\xi]_i$ is proportional to how much power should be allocated for $\mathbf{w}_i$. Thus, for convenience we define $[\xi]_i = \delta_i/\|[\mathbf{C}_w]_{:,i}\|^2$, where $1 \geq \delta_i \geq 0$ determines the exact portion of the total transmitted power P in (1) dedicated for the i-th codeword. Thus, the first part of the proposition is proved.

Next, to obtain the corresponding BB and EM precoders, we use the equation (23) which establishes a relation between the vector $\mathbf{w}_i$ and $\mathbf{E}_i^{\mathsf{T}}, \mathbf{f}_i$. According to the definition of $\mathbf{E}_i$, we obtain the following equation:

$$[\mathbf{w}_i]_{(m-1)Q+1:mQ} = [\mathbf{f}_i]_m\mathbf{e}_{m,i}, \tag{71}$$

for $m = 1, \ldots, M$. After substituting (70) in (71): $[\mathbf{f}_i]_m\mathbf{e}_{m,i} = \frac{\delta_i\mathbf{c}_m^{(i)}(\boldsymbol{\theta})}{\|[\mathbf{c}^{(i)}(\boldsymbol{\theta})\|}$. Since $\|\mathbf{e}_{m,i}\|^2 = 1$, we obtain the following unique family of solutions for $[\mathbf{f}_i]_m$ and $\mathbf{e}_{m,i}$:

$$[\mathbf{f}_i]_m = \sqrt{\delta_i}\frac{\|\mathbf{c}_m^{(i)}(\boldsymbol{\theta})\|}{\|\mathbf{c}^{(i)}(\boldsymbol{\theta})\|}e^{j\psi_{m,i}},\ \mathbf{e}_{m,i} = \frac{\mathbf{c}_m^{(i)}(\boldsymbol{\theta})}{\|\mathbf{c}_m^{(i)}(\boldsymbol{\theta})\|}e^{-j\psi_{m,i}}, \tag{72}$$

where $\{\psi_{m,i}\}_{m=1,i=1}^{M,3}$ are arbitrary phases.

Appendix D
Proof of Prop. 3

By replacing $\mathbf{q}_t(\boldsymbol{\theta})$ and $\mathbf{f}_t$ in (39) with $\mathbf{c}(\boldsymbol{\theta})$ and $\mathbf{w}_t$, the problem becomes similar to the synthesis case discussed in IV. Thus, by analogy, in a similar manner to Prop 1 and Prop. 2 (first part) for the synthesis case, we choose the following three codewords to achieve an approximate optimal performance:

$$\hat{\mathbf{f}}_i = \sqrt{\delta_i}\frac{\mathbf{q}^{(i)}(\boldsymbol{\theta})^*}{\|\mathbf{q}^{(i)}(\boldsymbol{\theta})\|}, \tag{73}$$

for $i = 1, 2, 3$, where

$$\mathbf{q}^{(1)}(\boldsymbol{\theta}) = \mathbf{q}_1(\boldsymbol{\theta}),\ \mathbf{q}^{(2)}(\boldsymbol{\theta}) = \frac{\partial\,\mathbf{q}_2(\boldsymbol{\theta})}{\partial\theta^{\text{el}}},\ \mathbf{q}^{(3)}(\boldsymbol{\theta}) = \frac{\partial\,\mathbf{q}_3(\boldsymbol{\theta})}{\partial\theta^{\text{az}}} \tag{74}$$

After substituting (16) in (74) and using (38), the equations (41) are obtained, which completes the proof.

REFERENCES

[1] R. Wang *et al.*, "Electromagnetically reconfigurable fluid antenna system for wireless communications: Design, modeling, algorithm, fabrication, and experiment," *IEEE Journal on Selected Areas in Communications., early access*, 2025.

[2] K.-K. Wong *et al.*, "Fluid antenna system—part II: Research opportunities," *IEEE Communications Letters*, vol. 27, no. 8, pp. 1924–1928, 2023.

[3] K. Ying *et al.*, "Reconfigurable massive MIMO: Precoding design and channel estimation in the electromagnetic domain," *IEEE Transactions on Communications*, vol. 73, no. 5, pp. 3423–3440, 2025.

[4] W. Chen *et al.*, "5G-advanced toward 6G: Past, present, and future," *IEEE Journal on Selected Areas in Communications*, vol. 41, no. 6, pp. 1592–1619, 2023.

[5] K.-K. Wong *et al.*, "Fluid antenna systems," *IEEE Transactions on Wireless Communications*, vol. 20, no. 3, pp. 1950–1962, 2021.

[6] A. Fadakar *et al.*, "Mutual coupling-aware localization for RIS-assisted ISAC systems," *IEEE Transactions on Cognitive Communications and Networking*, vol. 11, no. 5, pp. 2938–2954, 2025.

[7] P. Zheng *et al.*, "Tri-hybrid multi-user precoding using pattern-reconfigurable antennas: Fundamental models and practical algorithms," *arXiv preprint arXiv:2505.08938*, 2025.

[8] Y. Zhang *et al.*, "Joint bistatic positioning and monostatic sensing: Optimized beamforming and performance tradeoff," *IEEE Transactions on Cognitive Communications and Networking*, vol. 11, no. 5, pp. 2834–2847, 2025.

[9] W. K. New *et al.*, "A tutorial on fluid antenna system for 6G networks: Encompassing communication theory, optimization methods and hardware designs," *IEEE Communications Surveys & Tutorials*, vol. 27, no. 4, pp. 2325–2377, 2025.

[10] L. Zhu *et al.*, "A tutorial on movable antennas for wireless networks," *IEEE Communications Surveys & Tutorials*, vol. 28, pp. 3002–3054, 2026.

[11] Y. Zhang *et al.*, "Movable antenna-aided hybrid beamforming for multi-user communications," *IEEE Transactions on Vehicular Technology*, vol. 74, no. 6, pp. 9899–9903, 2025.

[12] ——, "6DMA-aided hybrid beamforming with joint antenna position and orientation optimization," *arXiv preprint arXiv:2412.17088*, 2024.

[13] L. Zhu *et al.*, "Historical review of fluid antenna and movable antenna," *arXiv preprint arXiv:2401.02362*, 2024.

[14] J. O. Martinez *et al.*, "Toward liquid reconfigurable antenna arrays for wireless communications," *IEEE Communications Magazine*, vol. 60, no. 12, pp. 145–151, 2022.

[15] C. Borda-Fortuny *et al.*, "Low-cost 3D-printed coupling-fed frequency agile fluidic monopole antenna system," *IEEE Access*, vol. 7, pp. 95 058–95 064, 2019.

[16] L. Song *et al.*, "Wideband frequency reconfigurable patch antenna with switchable slots based on liquid metal and 3-D printed microfluidics," *IEEE Transactions on Antennas and Propagation*, vol. 67, no. 5, pp. 2886–2895, 2019.

[17] D. Rodrigo *et al.*, "Frequency, radiation pattern and polarization reconfigurable antenna using a parasitic pixel layer," *IEEE Transactions on Antennas and Propagation*, vol. 62, no. 6, pp. 3422–3427, 2014.

[18] J. Zhang *et al.*, "A novel pixel-based reconfigurable antenna applied in fluid antenna systems with high switching speed," *IEEE Open Journal of Antennas and Propagation*, vol. 6, no. 1, pp. 212–228, 2025.

[19] M. Liu *et al.*, "Tri-timescale beamforming design for tri-hybrid architectures with reconfigurable antennas," *arXiv preprint arXiv:2503.03620*, 2025.

[20] Z. Han *et al.*, "Characteristic mode analysis of ESPAR for single-RF MIMO systems," *IEEE Transactions on Wireless Communications*, vol. 20, no. 4, pp. 2353–2367, 2021.

[21] P. Lotfi *et al.*, "Printed endfire beam-steerable pixel antenna," *IEEE Transactions on Antennas and Propagation*, vol. 65, no. 8, pp. 3913–3923, 2017.

[22] H. Xu *et al.*, "The future is fluid: Revolutionizing DOA estimation with sparse fluid antennas," *arXiv preprint arXiv:2508.10826*, 2025.

[23] ——, "Fluid antenna enabled direction-of-arrival estimation under time-constrained mobility," *arXiv preprint arXiv:2508.10820*, 2025.

[24] Z. Li *et al.*, "Movable antennas enabled ISAC systems: Fundamentals, opportunities, and future directions," *IEEE Wireless Communications*, pp. 1–8, 2025.

[25] W. Lyu *et al.*, "Movable antenna enabled integrated sensing and communication," *IEEE Transactions on Wireless Communications*, vol. 24, no. 4, pp. 2862–2875, 2025.

[26] J. Ding *et al.*, "Movable antenna-aided near-field integrated sensing and communication," *IEEE Transactions on Wireless Communications*, vol. 25, pp. 493–508, 2026.

[27] T. Hao *et al.*, "Fluid-antenna enhanced ISAC: Joint antenna positioning and dual-functional beamforming design under perfect and imperfect CSI," *IEEE Transactions on Vehicular Technology*, pp. 1–16, 2025.

[28] C. Wang *et al.*, "Fluid antenna system liberating multiuser MIMO for ISAC via deep reinforcement learning," *IEEE Transactions on Wireless Communications*, vol. 23, no. 9, pp. 10 879–10 894, 2024.

[29] E. Taillefer *et al.*, "Direction-of-arrival estimation using radiation power pattern with an ESPAR antenna," *IEEE Transactions on Antennas and Propagation*, vol. 53, no. 2, pp. 678–684, 2005.

[30] R. Qian *et al.*, "Direction-of-arrival estimation with single-RF ESPAR antennas via sparse signal reconstruction," in *2015 IEEE 16th International Workshop on Signal Processing Advances in Wireless Communications (SPAWC)*, 2015, pp. 485–489.

[31] ——, "Direction-of-arrival estimation with ESPAR antennas using Bayesian compressive sensing," in *2016 IEEE International Conference on Acoustics, Speech and Signal Processing (ICASSP)*, 2016, pp. 3076–3080.

[32] L. Kulas, "Simple 2-D direction-of-arrival estimation using an ESPAR antenna," *IEEE Antennas and Wireless Propagation Letters*, vol. 16, pp. 2513–2516, 2017.

[33] ——, "RSS-based DoA estimation using ESPAR antennas and interpolated radiation patterns," *IEEE Antennas and Wireless Propagation Letters*, vol. 17, no. 1, pp. 25–28, 2018.

[34] M. Tarkowski *et al.*, "RSS-based DoA estimation for ESPAR antennas using support vector machine," *IEEE Antennas and Wireless Propagation Letters*, vol. 18, no. 4, pp. 561–565, 2019.

[35] O. Bshara *et al.*, "Noncooperative sub-6GHz reconfigurable antenna DoA estimation to aid mmwave analog beamforming: Algorithm and measurements," *IEEE Access*, vol. 9, pp. 101 876–101 885, 2021.

[36] M. Rzymowski *et al.*, "Single-anchor indoor localization using ESPAR antenna," *IEEE Antennas and Wireless Propagation Letters*, vol. 15, pp. 1183–1186, 2016.

[37] M. Groth *et al.*, "Fast calibration-free single-anchor indoor localization based on limited number of ESPAR antenna radiation patterns," in *2023 17th European Conference on Antennas and Propagation (EuCAP)*, 2023, pp. 1–5.

[38] A. Fadakar *et al.*, "Multi-RIS-assisted 3D localization and synchronization via deep learning," *IEEE Open Journal of the Communications Society*, vol. 5, pp. 3299–3314, 2024.

[39] M. Costa *et al.*, "Unified array manifold decomposition based on spherical harmonics and 2-D fourier basis," *IEEE Transactions on Signal Processing*, vol. 58, no. 9, pp. 4634–4645, 2010.

[40] C. Zhang *et al.*, "Compact millimeter wave massive MIMO system utilizing ESPAR," *IEEE Transactions on Communications*, vol. 73, no. 11, pp. 10 262–10 276, 2025.

[41] A. Fascista *et al.*, "RIS-aided joint localization and synchronization with a single-antenna receiver: Beamforming design and low-complexity estimation," *IEEE Journal of Selected Topics in Signal Processing*, vol. 16, no. 5, pp. 1141–1156, 2022.

[42] A. Fadakar *et al.*, "Near-field RIS-assisted localization under mutual coupling," in *2025 IEEE International Conference on Communications Workshops (ICC Workshops)*, 2025, pp. 1470–1475.

[43] S. Boyd, "Convex optimization," *Cambridge UP*, 2004.

[44] A. Nemirovski, "Interior point polynomial time methods in convex programming," *Lecture notes*, vol. 42, no. 16, pp. 3215–3224, 2004.

[45] M. F. Keskin *et al.*, "Optimal spatial signal design for mmWave positioning under imperfect synchronization," *IEEE Transactions on Vehicular Technology*, vol. 71, no. 5, pp. 5558–5563, 2022.

[46] A. Fadakar *et al.*, "Deep learning aided multi-source passive 3D AOA wireless positioning using a moving receiver: A low complexity approach," *Ad Hoc Networks*, vol. 154, p. 103382, 2024.

[47] ——, "Deep learning based 2D-DOA estimation using l-shaped arrays," *Journal of the Franklin Institute*, vol. 361, no. 6, p. 106743, 2024.

[48] Z. Muhi-Eldeen *et al.*, "Modelling and measurements of millimetre wavelength propagation in urban environments," *IET microwaves, antennas & propagation*, vol. 4, no. 9, pp. 1300–1309, 2010.

[49] W. Wang *et al.*, "Joint beam training and positioning for intelligent reflecting surfaces assisted millimeter wave communications," *IEEE Transactions on Wireless Communications*, vol. 20, no. 10, pp. 6282–6297, 2021.

[50] J. Li *et al.*, "Range compression and waveform optimization for MIMO radar: A cramer–rao bound based study," *IEEE Transactions on Signal Processing*, vol. 56, no. 1, pp. 218–232, 2008.